arXiv:1708.01535v2 [astro-ph.CO] 19 Dec 2017

Dark Energy Survey Year 1 Results:
Curved-Sky Weak Lensing Mass Map

C. Chang[1*], A. Pujol[2,3,4], B. Mawdsley[5], D. Bacon[5], J. Elvin-Poole[6], P. Melchior[7], A. Kovács[8], B. Jain[9], B. Leistedt[10,11], T. Giannantonio[12,13,14], A. Alarcon[4], E. Baxter[9], K. Bechtol[15], M. R. Becker[16,17], A. Benoit-Lévy[18,19,20], G. M. Bernstein[9], C. Bonnett[8], M. T. Busha[17], A. Carnero Rosell[21,22], F. J. Castander[4], R. Cawthon[1], L. N. da Costa[21,22], C. Davis[17], J. De Vicente[23], J. DeRose[16,17], A. Drlica-Wagner[24], P. Fosalba[4], M. Gatti[8], E. Gaztanaga[4], D. Gruen[11,17,25], J. Gschwend[21,22], W. G. Hartley[19,26], B. Hoyle[14], E. M. Huff[27], M. Jarvis[9], N. Jeffrey[19], T. Kacprzak[26], H. Lin[24], N. MacCrann[28,29], M. A. G. Maia[21,22], R. L. C. Ogando[21,22], J. Prat[8], M. M. Rau[14], R. P. Rollins[6], A. Roodman[17,25], E. Rozo[30], E. S. Rykoff[17,25], S. Samuroff[6], C. Sánchez[8], I. Sevilla-Noarbe[23], E. Sheldon[31], M. A. Troxel[28,29], T. N. Varga[14,32], P. Vielzeuf[8], V. Vikram[33], R. H. Wechsler[16,17,25], J. Zuntz[34], T. M. C. Abbott[35], F. B. Abdalla[19,36], S. Allam[24], J. Annis[24], E. Bertin[18,20], D. Brooks[19], E. Buckley-Geer[24], D. L. Burke[17,25], M. Carrasco Kind[37,38], J. Carretero[8], M. Crocce[4], C. E. Cunha[17], C. B. D'Andrea[9], S. Desai[39], H. T. Diehl[24], J. P. Dietrich[14,40], P. Doel[19], J. Estrada[24], A. Fausti Neto[21], E. Fernandez[8], B. Flaugher[24], J. Frieman[1,24], J. García-Bellido[41], R. A. Gruendl[37,38], G. Gutierrez[24], K. Honscheid[28,29], D. J. James[42], T. Jeltema[43], M. W. G. Johnson[38], M. D. Johnson[38], S. Kent[1,24], D. Kirk[19], E. Krause[17], K. Kuehn[44], S. Kuhlmann[33], O. Lahav[19], T. S. Li[24], M. Lima[21,45], M. March[9], P. Martini[28,29], F. Menanteau[37,38], R. Miquel[8,46], J. J. Mohr[14,32,40], E. Neilsen[24], R. C. Nichol[5], D. Petravick[38], A. A. Plazas[27], A. K. Romer[47], M. Sako[9], E. Sanchez[23], V. Scarpine[24], M. Schubnell[48], M. Smith[49], R. C. Smith[35], M. Soares-Santos[24], F. Sobreira[21,50], E. Suchyta[51], G. Tarle[48], D. Thomas[5], D. L. Tucker[24], A. R. Walker[35], W. Wester[24], Y. Zhang[24]

(DES Collaboration)

The authors' affiliations are shown in Appendix D.
e-mail address: chihway@kicp.uchicago.edu

21 December 2017

ABSTRACT

We construct the largest curved-sky galaxy weak lensing mass map to date from the DES first-year (DES Y1) data. The map, about 10 times larger than previous work, is constructed over a contiguous $\approx 1,500$ deg^2, covering a comoving volume of ≈ 10 Gpc^3. The effects of masking, sampling, and noise are tested using simulations. We generate weak lensing maps from two DES Y1 shear catalogs, METACALIBRATION and IM3SHAPE, with sources at redshift $0.2 < z < 1.3$, and in each of four bins in this range. In the highest signal-to-noise map, the ratio between the mean signal-to-noise in the E-mode and the B-mode map is $\sim$1.5 ($\sim$2) when smoothed with a Gaussian filter of $\sigma_G = 30$ (80) arcminutes. The second and third moments of the convergence κ in the maps are in agreement with simulations. We also find no significant correlation of κ with maps of potential systematic contaminants. Finally, we demonstrate two applications of the mass maps: (1) cross-correlation with different foreground tracers of mass and (2) exploration of the largest peaks and voids in the maps.

Key words: gravitational lensing: weak, cosmology: dark matter, surveys

1 INTRODUCTION

One way to map the mass distribution of the Universe is by using the technique of weak gravitational lensing. (Kaiser & Squires 1993; Massey et al. 2007; Van Waerbeke et al. 2013; Vikram et al. 2015; Chang et al. 2015; Oguri et al. 2017). The motivations for generating these mass maps using weak lensing are twofold. First, it is easy to pick out distinct features and understand the qualitative characteristics of the mass distribution from maps. Second, as the

maps ideally preserve the full, uncompressed information for the field, they enable the extraction of non-Gaussian information beyond the standard two-point statistics used in cosmology (e.g. Abbott et al. 2016; Kwan et al. 2017; Hildebrandt et al. 2017). These non-Gaussian statistics are being explored using 3-point statistics (Cooray & Hu 2001; Dodelson & Zhang 2005), peak counts (Dietrich & Hartlap 2010; Kratochvil et al. 2010; Kacprzak et al. 2016), and the full Probability Density Function (PDF) of the map (Clerkin et al. 2015; Patton et al. 2016). As the statistical uncertainties in the current and future data sets decrease, we expect these higher-order statistics to offer new constraints that are complementary to the more traditional two-point approaches.

Physically, a weak lensing mass map, or convergence map, represents the integrated total matter density along the line-of-sight, weighted by a broad lensing kernel that peaks roughly half-way between the observer and the source galaxies from which the measurement is made. Since lensing does not distinguish between the species and dynamical state of the mass, or the "lens", one can directly probe mass with weak lensing, which is a key difference from maps constructed from biased tracers of mass such as galaxies. The theoretical framework of constructing weak lensing convergence maps from the weak lensing observable, shear, has been developed since Kaiser & Squires (1993, hereafter KS) and Schneider (1996). Shear and convergence are second derivatives of the same lensing potential field, which makes it possible to convert between them up to a constant.

Small-field weak lensing mass maps have been commonly used in galaxy cluster fields to study the detailed structure of the cluster mass distribution and compare with the distribution of baryonic matter (Clowe et al. 2006; von der Linden et al. 2014; Melchior et al. 2015). These maps have relatively high signal-to-noise because the cluster lensing signal is ~ 10 times larger than the lensing signal from the large-scale structure (Bartelmann & Schneider 2001), and the information about the fields was obtained using deep imaging to achieve a high number density of source galaxies for weak lensing measurements. A number of algorithms beyond KS were developed to specifically tackle the mass reconstruction with clusters and have been successfully implemented on data (Seitz et al. 1998; Marshall et al. 2002; Leonard et al. 2014).

Wide-field convergence maps, on the other hand, have only been constructed recently, thanks to the development of dedicated weak lensing surveys that cover patches of sky on the order of hundreds of square degrees or larger. This includes the Canada-France-Hawaii Telescope Lensing Survey (CFHTLenS, Erben et al. 2013), the KIlo-Degree Survey (KIDS, de Jong et al. 2015), the Hyper SuprimeCam Survey (HSC, Aihara et al. 2017) and the Dark Energy Survey (DES, Flaugher 2005). Van Waerbeke et al. (2013) was the first to study in detail these wide-field weak lensing mass maps in four fields (adding up to a total of 154 deg^2) of the CFHTLenS data, including the noise properties, high-order moments, and the cross-correlation with galaxies. In Vikram et al. (2015) and Chang et al. (2015), we carried out a similar analysis with early DES Science Verification (SV) data using a 139 deg^2 contiguous region of the sky. Recent work from HSC (Mandelbaum et al. 2017; Oguri et al. 2017) also carried out an analysis of mass map reconstruction using the HSC data in both 2D and 3D. Although the area of these maps are not as large (the total area of the data set is 136.9 deg^2, split into six separate fields), the number density of the sources is several times larger than in the other data sets (25 galaxies per arcmin^2), which allows for reconstruction on much smaller scales. Oguri et al. (2017) looked at cross-correlation of the mass maps with galaxy distributions and several systematics tests. All three

studies described above use the KS method under flat-sky approximation, and show that the mass maps contain significant extractable cosmological information.

Continuing from the SV work described above to the first year of DES data (DES Y1), we present in this paper a weak lensing mass map of $\sim 1,500$ deg^2, more than ten times larger than the SV map. A few advances over the SV studies were made: First, given the large area of the mass map on the sky, it was necessary to go beyond the flat-sky approximation and employ curved-sky estimators. The implementation of the curved-sky reconstruction borrows from tools developed for CMB polarisation analyses and has been studied in detail in the context of weak lensing mass mapping and cosmic shear (Heavens 2003; Castro et al. 2005; Heavens et al. 2006; Kitching et al. 2014; Leistedt et al. 2017; Wallis et al. 2017). The first all sky curved weak lensing maps constructed from simulations were presented in Fosalba et al. (2008), which was an extension from the work on constructing mock galaxy catalogs in Gaztanaga & Bernardeau (1998). Second, we move from a single redshift bin to multiple redshift bins, a first step towards constructing a 3D weak lensing map. These tomographic bins match those used in the DES Y1 cosmology analysis, thus making our maps very complementary to the series of DES Y1 papers that focus on two-point statistics (DES Collaboration et al. 2017; Troxel et al. 2017; Prat et al. 2017; MacCrann et al. 2017). Specifically, this paper presents the spatial configuration and phase information of the data that goes into these cosmological analyses. Finally, we explore for the first time the possibility of constructing the lensing potential and deflection fields. These fields are commonly studied in the CMB lensing community, but seldom constructed and visualised using measurements of galaxy lensing except in some theoretical studies (Vallinotto et al. 2007; Dodelson et al. 2008; Chang & Jain 2014). The primary reason that potential and deflection fields are seldom used in galaxy lensing is that the information of the potential and deflection fields are on scales much larger (or lower ℓ modes) than the convergence field. This means that in previous smaller data sets, there is not enough low ℓ information in the data to reconstruct the potential and deflection fields. However, with the wide-field data used in this work, we are just beginning to enter the era where the reconstruction is not dominated by noise and interesting applications can be explored. For example, with an accurate deflection field, one can "delens" the galaxy fields and move the observed galaxy positions back to their unlensed position, which would improve measurements such as galaxy-galaxy lensing (Chang & Jain 2014). Similarly, having a good estimate of the lensing potential could in principle provide foreground information for delensing the CMB (Marian & Bernstein 2007; Manzotti et al. 2017; Yu et al. 2017).

This paper is organised as follows. In Sec. 2 we introduce the formalism used for constructing the curved-sky convergence map from shear maps. In Sec. 3, the data and simulations used in this paper are described. We then outline in Sec. 4 the practical procedure of constructing the maps from the DES Y1 shear catalogs. In Sec. 5 we present a series of tests using simulated data to quantitatively understand the performance of the map-making method as well as how that method interacts with the different sources of noise in the data. We then present our final DES Y1 mass maps in Sec. 6 for different redshift bins and test for residual systematic effects by cross-correlating the maps with observational quantities. We follow up with two applications of the mass maps in Sec. 7: (1) cross-correlation of the mass maps with different foreground galaxy samples, and (2) examination of the largest peaks and voids in the maps. We conclude in Sec. 8. In Appendix A we investigate

the different approaches of masking and their effect on the reconstruction. In Appendix B we demonstrate the possibility of reconstructing the weak lensing potential and deflection maps in addition to the convergence map, which will become more interesting in future datasets as the sky coverage increases. Finally in Appendix C we present convergence maps from the IM3SHAPE shear catalog (in addition to the maps from the METACALIBRATION shear catalog presented in the main text) to show the consistency between the catalogs.

2 FORMALISM

As mentioned in Sec. 1, the construction of convergence (κ) maps from shear (γ) maps in data has been done assuming the flat-sky approximation in most previous work (Van Waerbeke et al. 2013; Vikram et al. 2015; Chang et al. 2015) due to the relatively small sky coverage involved. In fact, as shown in Wallis et al. (2017), the gain in moving from flat-sky to curved-sky is very marginal in the case where the data is on the order of 100 deg^2. In this paper, our data set is sufficiently large to warrant a curved-sky treatment, which also prepares us for future, even larger, data sets. The fundamental mathematical operation that we are interested in is to decompose a spin-2 field (γ) into a curl-free component and a divergence-free component. The curl-free component corresponds to the convergence signal, which is also referred to as the E-mode convergence field κ_E. The divergence-free component, which we refer to as κ_B, is expected to be negligible compared to κ_E for gravitational lensing, but can arise from noise and systematics in the shear estimates. Mathematically, this operation is the same as the classical Helmholtz decomposition, but generalised onto the spherical coordinates. We sketch below the formalism of converting between the κ and γ maps as well as the deflection field $\boldsymbol{\eta}$ and the potential field ψ. For detailed derivations, we refer the reader to Bartelmann (2010); Castro et al. (2005); Wallis et al. (2017).

Consider the 3D Newtonian potential Ψ defined at every given comoving distance χ and angular position (θ, ϕ) on the sky. The effective lensing potential ψ is defined by projecting Ψ along the line-of-sight. That is (Bartelmann & Schneider 2001),

$$\psi(\chi_s, \theta, \phi) = 2 \int d\chi' \frac{f_K(\chi_s - \chi')}{f_K(\chi') f_K(\chi_s)} \Psi(\chi', \theta, \phi), \tag{1}$$

where f_K depends on the curvature k of the Universe: $f_K(\chi) = \sin\chi, \chi, \sinh\chi$ for closed ($k = 1$), flat ($k = 0$) and open ($k = -1$) universe respectively. The 3D potential is related to the distribution of the matter overdensity $\delta(\chi, \theta, \phi)$ via the Poisson equation

$$\nabla_\chi^2 \Psi(\chi, \theta, \phi) = \frac{3\Omega_m H_0^2}{2a} \delta(\chi, \theta, \phi), \tag{2}$$

where Ω_m is the total matter density today, H_0 is the Hubble constant today, and $a = 1/(1+z)$ is the scale factor. Note that the gradient ∇_χ is taken in the comoving radial direction.

Expanding the lensing potential at a given comoving distance χ in spherical harmonics, we have

$$\psi(\chi) = \sum_{\ell m} \psi_{\ell m}(\chi) \, _0Y_{\ell m}(\theta, \phi),$$

$$\psi_{\ell m}(\chi) = \int d\Omega \psi(\chi) \, _0Y_{\ell m}^*(\theta, \phi), \tag{3}$$

where $_0Y_{\ell m}$ are the spin-0 spherical harmonic basis set and $\psi_{\ell m}(\chi)$ is the coefficient associated with $_0Y_{\ell m}$ at χ. Below we will omit the χ reference in our notation for simplicity, but note that these equations apply to the fields on a given redshift shell.

To derive the spherical harmonic representation of shear and convergence, we have

$$\kappa = \frac{1}{4}(\eth\,\bar{\eth} + \bar{\eth}\,\eth)\psi, \tag{4}$$

$$\gamma = \gamma^1 + i\gamma^2 = \frac{1}{2}\eth\,\eth\,\psi, \tag{5}$$

where $\eth$ and $\bar{\eth}$ are the raising and lowering operators that act on spin-weighted spherical harmonics, $_sY_{\ell m}$ and follow a certain set of rules (see e.g., Castro et al. 2005, for details). We can now define the spherical representation of the convergence field and the shear field to be

$$\kappa = \kappa_E + i\kappa_B = \sum_{\ell m} (\hat{\kappa}_{E,\ell m} + i\hat{\kappa}_{B,\ell m}) \, _0Y_{\ell m}, \tag{6}$$

and

$$\gamma = \gamma^1 + i\gamma^2 = \sum_{\ell m} \hat{\gamma}_{\ell m} \, _2Y_{\ell m}. \tag{7}$$

Here $_2Y_{\ell m}$ are spin-2 spherical harmonics. From Eq. (4) and Eq. (5) it follows that

$$\hat{\kappa}_{E,\ell m} + i\hat{\kappa}_{B,\ell m} = -\frac{1}{2}\ell(\ell+1)\psi_{\ell m}, \tag{8}$$

$$\begin{aligned}\hat{\gamma}_{\ell m} &= \hat{\gamma}_{E,\ell m} + i\hat{\gamma}_{B,\ell m} \\ &= \frac{1}{2}[\ell(\ell+1)(\ell-1)(\ell+2)]^{\frac{1}{2}}\psi_{\ell m} \\ &= -\sqrt{\frac{(\ell+2)(\ell-1)}{\ell(\ell+1)}}(\hat{\kappa}_{E,\ell m} + i\hat{\kappa}_{B,\ell m}). \end{aligned} \tag{9}$$

That is, one can convert between the three fields: κ, γ and ψ by manipulating their spherical harmonics decompositions. The mathematical operation described above is entirely analogous to a description of linear polarisation such as that in the CMB polarisation measurements. In this analogy, the Q and U Stokes parameters correspond to the γ^1 and γ^2. In the flat-sky limit, we have $\eth \to \partial$ and the decomposition into spherical harmonics is replaced by the Fourier transform, $\Sigma \psi_{\ell m} Y_{\ell m} \to \int \frac{d^2\ell}{(2\pi)^2} \psi(\ell) e^{i\boldsymbol{\ell}\cdot\boldsymbol{\theta}}$. The above equations then reduce to the usual KS formalism.

One can derive the lensing deflection field $\boldsymbol{\eta}$ in a similar fashion. The lensing deflection field is defined as the first derivative of the lensing potential

$$\boldsymbol{\eta} = \eta^1 + i\eta^2 = \eth\,\psi, \tag{10}$$

so the deflection field is a spin-1 field and can be expressed as

$$\boldsymbol{\eta} = \eta^1 + i\eta^2 = \sum_{\ell m} \hat{\eta}_{\ell m} \, _1Y_{\ell m}. \tag{11}$$

Carrying through the derivation, we get

$$\hat{\eta}_{\ell m} = [\ell(\ell+1)]^{\frac{1}{2}}\psi_{\ell m}, \tag{12}$$

which is again related to the other lensing quantities via a simple linear operation in the spin-harmonic space. That is, once γ is measured, the other fields (κ, $\boldsymbol{\eta}$ and ψ) can be constructed using the formalism described above.

From Eq. (8) and Eq. (9) we observe from which ℓ modes κ, $\boldsymbol{\eta}$ and ψ receive their dominant contributions: ψ receives most contribution from the lowest ℓ modes, $\boldsymbol{\eta}$ receives contribution from slightly higher ℓ modes, and κ receives contribution from even higher ℓ modes. Therefore, κ is more strongly influenced by the

smaller scale effects (e.g. noise) and ψ is affected by large scale effects (e.g. masking). This can also be seen from the fact that the κ (η) field is derived from applying a Laplacian (derivative) operator on the ψ field, which means that the power spectrum of κ (η) scales like ℓ^4 (ℓ^2) times the power spectrum of ψ. The main focus of this paper is to construct the κ map. However, we also explore the construction of the η and ψ in Appendix B to show that the quality of the reconstruction for these fields is indeed sensitive to the mask on large-scales and less sensitive to shape noise on small scales. We also show that with the 1,500 deg^2 sky coverage of DES Y1, reconstructing the η and ψ maps are just starting to be interesting.

In practice, the main observable for weak lensing is the galaxy shape ε, which in the weak lensing regime, is a noisy estimate of γ. When averaged over a large number of galaxies, $\langle \varepsilon \rangle \approx g = \frac{\gamma}{1-\kappa}$, where g is the reduced shear. As $\kappa \ll 1$ in the weak lensing regime, $\varepsilon \approx \gamma$. The noise in ε is dominated by the intrinsic shape of the galaxies, or "shape noise", but also includes measurement noise. That is,

$$\varepsilon = \gamma + \varepsilon_{\text{int}} + \varepsilon_{\text{m}}, \tag{13}$$

where ε_{int} is the intrinsic shape of the galaxy and ε_{m} is the error on the measured shape due to the measurement. One often quantifies the combined effect of ε_{int} and ε_{m} using σ_ε, the standard deviation of the distribution of $\varepsilon_{\text{int}} + \varepsilon_{\text{m}}$. As we will see in Sec. 4, one needs to average ε over a large number of galaxies to suppress this noise. Note that here we have not considered the effect of intrinsic alignment (IA, Troxel & Ishak 2015; Blazek et al. 2015), where $\langle \varepsilon \rangle \approx g$ no longer holds.

3   DATA AND SIMULATIONS

DES is an ongoing wide-field galaxy and supernova survey that began in August 2013 and aims to cover a total of 5000 deg^2 in five filter bands (*grizY*) to a final median depth of $g \sim 24.45$, $r \sim 24.3$, $i \sim 23.5$, $z \sim 22.9$, $Y \sim 21.7$ (10-σ PSF limiting magnitude, see Dark Energy Survey Collaboration et al. 2016) at the end of the survey. The survey instrument is the Dark Energy Camera (Flaugher et al. 2015) installed on the 4m Blanco telescope at the Cerro Tololo Inter-American Observatory (CTIO) in Chile. This work is based on the DES first-year cosmology data set (Y1A1 GOLD) including photometrically calibrated object catalogs and associate ancillary coverage and depth maps (Drlica-Wagner et al. 2017). We focus on the Southern footprint of the DES Y1 data, which overlaps with the South Pole Telescope survey (Carlstrom et al. 2011). This is the largest contiguous area in the Y1 data set and ideal for constructing weak lensing mass maps. We briefly describe below the data products and simulations used in this work.

3.1   Photometric redshift (photo-*z*) catalog

We use the photometric redshifts (photo-*z*'s) derived using a code closely following the Bayesian Photometric Redshifts (BPZ) algorithm developed in Benítez (2000) and Coe et al. (2006). BPZ is a template-fitting code using templates from Coleman et al. (1980); Kinney et al. (1996); Bruzual & Charlot (2003). The catalog generation in Y1 is similar to the SV analysis (Bonnett et al. 2016), but with several improvements described in Hoyle et al. (2017).

BPZ calculates a redshift PDF for each galaxy in that sample. The mean of this PDF, z_{mean}, is used to place source galaxies into redshift bins, while the $n(z)$ for each of the samples is estimated by randomly drawing a redshift from the PDF of each galaxy. These

$n(z)$'s are validated in Hoyle et al. (2017) using two orthogonal methodologies: comparison with precise redshifts and clustering-based inference, see Hoyle et al. (2017); Cawthon et al. (2017); Gatti et al. (2017); Davis et al. (2017).

3.2   Weak lensing shape catalogs

Two DES Y1 weak lensing shape catalogs are used in this paper — the METACALIBRATION catalog based on Huff & Mandelbaum (2017) and Sheldon & Huff (2017), and the IM3SHAPE catalog based on Zuntz et al. (2013). Both catalogs have been tested thoroughly in Zuntz et al. (2017, hereafter Z17). Given that the two algorithms are fundamentally different and that the pipelines were developed independently, obtaining consistent results from the two catalogs is a non-trivial test of the catalogs themselves.

Briefly, the METACALIBRATION algorithm relies on a self-calibration framework using the data itself, instead of a large number of image simulations as is used in many other algorithms (e.g. IM3SHAPE, Bruderer et al. 2016; Fenech Conti et al. 2016). The basic idea is to apply a small, known shear on the *deconvolved* galaxy images in different directions and re-measure the post-shear reconvolved galaxy shapes. Since the input shear is known, the change in the measured galaxy shapes due to the artificial shearing gives a direct measure of how the shear estimators responds to shear. This quantity is referred to as the *response*. In addition, selection effects[1] can be easily corrected in this framework by measuring the response for the full sample and for the subsample. The final signal-to-noise and size selection for the catalog is S/N>10 and $T/T_{PSF} > 0.5$ (T and T_{PSF} are the sizes of the galaxy and the PSF, respectively). Following Z17, the residual systematic errors are quoted in terms of m (the multiplicative bias), α (the additive bias associated with the PSF model ellipticity ε_{PSF}) and β (the additive bias associated with the errors on the PSF model ellipticity $\delta\varepsilon_{PSF}$). For METACALIBRATION, Z17 estimated $m = 0.0 \pm 1.2\%$, $\alpha \sim 0$, and $\beta \sim -1$. In Troxel et al. (2017), however, it is found that the β correction has very little effect on the final measurements. We therefore do not correct for β when making the mass maps. We have also checked that setting $\beta = -1$ leads to negligible changes in the second moments of the map. This selection gives a total of $\sim 34,800,000$ galaxies in the full Y1 catalog. The shear measurement method in METACALIBRATION is based on the NG-MIX method (Sheldon 2014). The full implementation of META-CALIBRATION is publicly available and hosted under the NGMIX code repository[2].

The IM3SHAPE algorithm is one of the algorithms also used in the DES SV analyses (Jarvis et al. 2015). It is a maximum likelihood fitting code using the Levenberg-Marquardt minimisation that models the galaxies either as an exponential disk or a de Vaucouleurs profile — fitting is done with both models and the one with a better likelihood goes into the final catalog. Calibration of bias in the shear estimate associated with noise (Kacprzak et al. 2012; Refregier et al. 2012) is based on the image simulation package GALSIM[3], but is significantly more complex and incorporates many effects seen in the DES Y1 data as described in Z17 and Samuroff et al. (2017). The final signal-to-noise and size selections are $12 < S/N < 200$ and $1.13 < R_{gp}/R_p < 3$, where R_{gp} is

---

[1] Here we refer to the fact that the response is different when one selects a subsample of the galaxies based on signal-to-noise, sizes, redshift etc..
[2] https://github.com/esheldon/ngmix
[3] https://github.com/GalSim-developers/GalSim

the size of the galaxy and R_p is the size of the PSF. The catalog has an estimated $m \sim 0.0 \pm 2.5\%$, $\alpha \sim 0$, and $\beta \sim -1$. Similar to METACALIBRATION, we do not correct for β as Troxel et al. (2017) showed that the correction has a negligible effect on the measurements. The final catalog contains $\sim 21,900,000$ galaxies. The lower number relative to METACALIBRATION is due to the fact that IM3SHAPE operates on *r*-band images while METACALIBRATION use all images from the bands *r*,*i* and *z*. The IM3SHAPE code is publicly available[4].

Details for both shape catalogs and the tests performed on these catalogs can be found in Z17. We mainly show results for METACALIBRATION as it has the higher S/N, but also constructed IM3SHAPE maps and performed several systematics tests with these. Also, as noted above, we only use the SPT wide-field region with Dec< -35 as it has been the region where most testing was done for both the shear and the photo-*z* catalogs. We generate 5 maps for each catalog with different source z_{mean} selections: $0.2 < z < 1.3$, $0.2 < z < 0.43$, $0.43 < z < 0.63$, $0.63 < z < 0.9$, $0.9 < z < 1.3$. The first redshift bin combines galaxies in a broad redshift range to allow for a large source number density and therefore higher signal-to-noise for the mass maps. This is the map with which most quantitative studies are done in this paper. The other four redshift bins match those defined by Troxel et al. (2017), which are well-tested samples that meet the criterion for cosmic shear measurements. These maps are noisier, but allow us to explore the 3D tomographic aspect of the maps. Basic characteristics of the samples associated with the five maps are listed in Table 1 and Table 1 of Troxel et al. (2017).

Finally, both shear catalogs were blinded with a multiplicative factor during the entire analysis and only unblinded after all tests were finalised. See Z17 for the detailed blinding procedure.

3.3 Flux-limited galaxy catalog

In Sec. 7.1 we use a flux-limited galaxy sample as a tracer of the foreground mass of the mass maps. This sample is constructed to be a simple, clean flux-limited sample from the DES Y1 catalog (Drlica-Wagner et al. 2017), which is easier to compare with simulations as it puts less pressure on having other galaxy properties (colour, galaxy type) in the catalogs being matched to the data.

The catalog is built by applying the following selections to the DES Y1 catalog: $17.5 < i < 22.0$; $-1 < g-r < 3$, $-1 < r-i < 2.5$ and $-1 < i-z < 2$ to remove galaxies that potentially have very incorrect photo-*z*'s; `flags_gold`=0 to remove any blended, saturated, incomplete or problematic galaxies; `flags_badregion` ≤ 3 to remove problematic regions with e.g. high stellar contamination; `modest_class`=2 to select objects as galaxies. The full catalog contains $\sim 34,800,000$ objects, to which we further impose photo-*z* cuts to construct two samples, $0.2 < z < 0.4$ and $0.4 < z < 0.6$, together with a cut in Dec< -35 to select the SPT region. The two samples are then pixelated into HEALPIX maps of nside = 2048 using the associated masks, which is then used for computing the cross-correlation.

3.4 Simulations

Two types of simulations are used in this work to investigate the performance of the convergence map reconstruction and the effects of noise and masking. First, we generate fully sampled, Gaussian

maps with a given power spectrum using the `synfast` routine in HEALPIX (Górski et al. 2005). We use the software package COSMOSIS (Zuntz et al. 2015), which wraps around the CAMB software (Lewis & Bridle 2002), to generate the input power spectrum with the cosmological parameters: $\Omega_m = 0.295$, $\Omega_b = 0.047$, $\sigma_8 = 0.8$, $h = 0.69$, $n_s = 0.97$, and $w = -1$, although the particular details of the power spectrum are not very important for the tests we perform with these Gaussian simulations.

Second, we use the "Buzzard v1.3" mock galaxy catalogs based on N-body simulations as described in DeRose et al. (in prep). Briefly, three flat ΛCDM dark-matter-only N-body simulations were used, with 1050^3, 2600^3 and 4000^3 $Mpc^3 h^{-3}$ boxes and 1400^3, 2048^3 and 2048^3 particles, respectively. These boxes were run with LGADGET-2 (Springel 2005) with 2LPTIC initial conditions from (Crocce et al. 2006) and CAMB. The cosmology assumed was $\Omega_m = 0.286$, $\Omega_b = 0.047$, $\sigma_8 = 0.82$, $h = 0.7$, $n_s = 0.96$, and $w = -1$ (consistent with the best-fit cosmological parameters from the DES Y1 3×2-pt anaylsis (DES Collaboration et al. 2017). Particle lightcones were created from these boxes on the fly. Galaxies were then placed into the simulations and *grizY* magnitudes and shapes are assigned to each galaxy using the algorithm Adding Density Determined Galaxies to Lightcone Simulations (ADDGALS, Wechsler et al. in prep., DeRose et al. in prep.). Galaxies are assigned to dark matter particles and given r-band absolute magnitudes based on the distribution $p(\delta|M_r)$ measured from a high resolution simulation populated with galaxies using subhalo abundance matching (SHAM) (Conroy et al. 2006; Reddick et al. 2013), where δ is a large scale density proxy. Each galaxy is assigned an SED from SDSS DR6 (Cooper 2006) by finding neighbors in the space of $M_r - \Sigma_5$, where Σ_5 is the projected distance to the fifth nearest neighbor in redshift slices of width $\delta z = 0.02$. These SEDs are k-corrected and integrated over the appropriate bandpasses to generate *grizY* magnitudes.

Finally, the weak lensing parameters (κ and γ) in the simulations are based on the ray-tracing algorithm Curved-sky grAvitational Lensing for Cosmological Light conE simulatioNS (CALCLENS; Becker 2013) which builds on previous work by Gaztanaga & Bernardeau (1998) and Fosalba et al. (2008) to make all sky weak lensing maps from projected density fields in simulations. The ray-tracing resolution is accurate to $\simeq 6.4$ arcseconds. The catalogs were then post-processed and trimmed to match the quality of our data sample. This includes adding photometric noise using the DES Y1 depth map, running the same photo-*z* pipeline (BPZ) on the photometry, adding shape noise[5], imposing redshift, size, signal-to-noise cuts to match the shear catalog described in Sec. 3.2 (here the cuts are tailored to the METACALIBRATION catalog) and the flux-limited galaxy catalog described in Appendix 3.3. We note, however, that due to the setup of the simulation box, the footprint of the simulations is 26% smaller than the data, with the area of RA$> 100°$ removed. For the purpose of testing in this work, this does not impose a significant problem. We also note that the galaxy number density is 20% lower than our data set. To account for that, we scale the shape noise by a factor of $\sqrt{n_{\mathrm{gal,Buzzard}}/n_{\mathrm{gal,DES}}}$, where $n_{\mathrm{gal,Buzzard}}$ and $n_{\mathrm{gal,DES}}$ are the number density of source galaxies in the simulations and data respectively.

---

[4] https://bitbucket.org/joezuntz/im3shape/

[5] The Buzzard catalogs include shape noise that are modeled from external Subaru data sets, which are not fully representative of our data. In order to have a better matching between simulation and data, we instead randomly draw the galaxy shapes from the METACALIBRATION catalog and add the simulated shear to the galaxy shape.

4   METHODOLOGY

We describe here the steps taken to construct the convergence map for the two shear catalogs. The only difference between the two catalogs is that different calibration schemes are applied to the shear estimates prior to making the maps.

All the maps are constructed using HEALPIX pixelisation, which is a natural choice for map making on the sphere and includes the necessary tools to manipulate the data on a sphere. This includes the decomposition of the spin fields into spin harmonics, which is essential for the transformation between shear γ, convergence κ, the lensing potential ψ and the deflection angle η, as we outlined in Sec. 2. We use a HEALPIX map of nside = 1024, which approximately corresponds to a mean pixel spacing of 3.44 arcminutes. This resolution is chosen based on the density of our source galaxies, and provides a good balance between the resolution of the map and the simplicity of the mask geometry. As the completeness of the source galaxies is not a concern here, no additional cuts on e.g. depth are needed beyond the selection from the shear catalog. The mask is defined to be 1 where there are galaxies within the pixel and 0 where there are no galaxies. This yields a total map area of $\sim 1,500$ deg^2, which appears larger than the naive footprint of our data in the SPT region ($\sim 1,300$ deg^2, Troxel et al. 2017). This is because we are using a coarser pixel resolution than what is used to estimate the footprint (nside = 4096). The final mask used in this paper still contains small "holes" in the otherwise contiguous footprint. We have considered interpolating over the holes to prevent edge effects, but found that these procedures make little difference in the reconstruction in terms of our metric defined in Sec. 5 (we give more details about these tests on Appendix A).

The first step in the reconstruction of the mass map involves making pixelised ellipticity (or shear estimate) maps ε^1 and ε^2 from the galaxy shape catalogs. To do this, we follow the procedure outlined in Section 7 of Z17 for calculating the mean shear per pixel. Note that both the response R for the METACALIBRATION catalog and the multiplicative noise-bias calibration (NBC) factor m for the IM3SHAPE catalog are noisy within each pixel of our maps. We therefore use the mean R and m values for each sample instead of calculating them in each pixel when constructing the maps. That is, for METACALIBRATION, we have

$$\varepsilon_i^\nu = \frac{\sum_j^{n_i} \varepsilon_{ij}^\nu}{n_i \bar{R}^\nu}, \quad \nu = 1, 2, \tag{14}$$

where n_i is the number of source galaxies in pixel i and ε_{ij}^ν is the shape estimate of each individual galaxy j in that pixel. $\bar{R}^\nu$ is the mean response of the full sample. The $\bar{R}^\nu$ values vary from ~ 0.7 to ~ 0.5 going from low to high redshift. Typically 1–2% of $\bar{R}^\nu$ comes from the correction of the selection effects. For the IM3SHAPE, we have

$$\varepsilon_i^\nu = \frac{1}{n_i(1+\bar{m})} \frac{\sum_{j=1}^{n_i}(\varepsilon_{ij}^\nu - c_{ij}^\nu)w_{ij}}{\sum_{j=1}^{n_i} w_{ij}}, \quad \nu = 1, 2, \tag{15}$$

where c_{ij}^ν and w_{ij} are the additive NBC factor and weight for galaxy j in pixel i, and $\bar{m}$ is the average multiplicative NBC factor for each sample. Typical m values range from -0.08 to -0.18 going from low to high redshift. We then subtract the mean shear for each sample from the maps as suggested by Z17 Section 7.1.

Next, we perform the spin transformation which converts the ellipticity maps (which combine to form a spin-2 field $\varepsilon^1 + i\varepsilon^2$) into a curl-free E-mode convergence map κ_E and a divergence-free B-mode convergence map κ_B. The HEALPIX functions map2alm performs this decomposition in spherical harmonic space and re-

Table 1. Characteristics of the source galaxy samples and the maps. The number preceding the semicolon is for the METACALIBRATION catalog while the number after the semicolon is for the IM3SHAPE catalog. $\bar{z}$ is the mean redshift estimate from BPZ for each sample, while σ_ε is the mean of σ_{ε^1} and σ_{ε^2}, the standard deviation of the weighted galaxy shapes reported from the catalogs (see last column in Table 1 of Troxel et al. 2017). The area of the map is $\sim 1,500$ deg^2 for both METACALIBRATION and IM3SHAPE, where the exact size changes slightly from different photo-z bins and shear catalogs. The HEALPIX maps have a resolution of nside = 1024.

Redshift range	$\bar{z}$	σ_ε
$0.2 < z < 1.3$	0.60; 0.56	0.28; 0.27
$0.2 < z < 0.43$	0.38; 0.36	0.26; 0.26
$0.43 < z < 0.63$	0.51; 0.52	0.30; 0.28
$0.63 < z < 0.9$	0.74; 0.75	0.27; 0.24
$0.9 < z < 1.3$	0.96; 1.03	0.28; 0.26

turns the E- and B-mode coefficients, which are equivalent to the $\hat{\gamma}_{E,\ell m}$ and $\hat{\gamma}_{B,\ell m}$ in Eq. (9). We calculate $\hat{\kappa}_{E,\ell m}$ and $\hat{\kappa}_{B,\ell m}$, then use the HEALPIX function alm2map to convert these coefficients back to the real space κ_E and κ_B maps. Similarly, ψ and η maps can be constructed using Eq. (9) and Eq. (12).

For all the convergence map visualisation in this paper, we further smooth the maps with a Gaussian kernel. The noise associated with each pixel after smoothing can be calculated through (Van Waerbeke et al. 2013)

$$\sigma_\kappa^2 = \frac{\sigma_{\varepsilon^1}^2 + \sigma_{\varepsilon^2}^2}{4\pi \sigma_G^2 n_{\rm gal}}, \tag{16}$$

where σ_{ε^1} and σ_{ε^2} are the standard deviation of the two components for the measured galaxy shapes, σ_G is the width of the Gaussian filter used to smooth the maps, and $n_{\rm gal}$ is the number density of the source galaxies.

Finally, for all measurements in this work, we estimate the error bars and the covariance matrix using a standard Jackknife approach. We divide the footprint into N_{JK} Jackknife regions using a kmeans clustering code[6] and divide the mask into N_{JK} approximately equal-area regions. Throughout this paper, we use $N_{JK} = 100$. For angular correlation measurements, a fast tree-based code TREECORR[7] is used.

5   SIMULATION TESTS

In this section we present a series of simulation tests to validate our procedure for map generation and quantify the uncertainties associated with the various source of systematics and noise. We start with an idealised setup of a Gaussian, fully-sampled, full-sky map in Sec. 5.1 to quantify the errors associated with the shear-to-convergence conversion alone, then we impose a DES Y1-like mask to investigate the degradation introduced by the mask. Next in Sec. 5.2, we repeat the tests in Sec. 5.1 with a mock galaxy catalog based on an N-body simulation. We test the effect of shot noise (finite sampling) and shape noise.

For both Sec. 5.1 and Sec. 5.2, we quantify the quality of the

---

[6] https://github.com/esheldon/kmeans_radec
[7] https://github.com/rmjarvis/TreeCorr/wiki
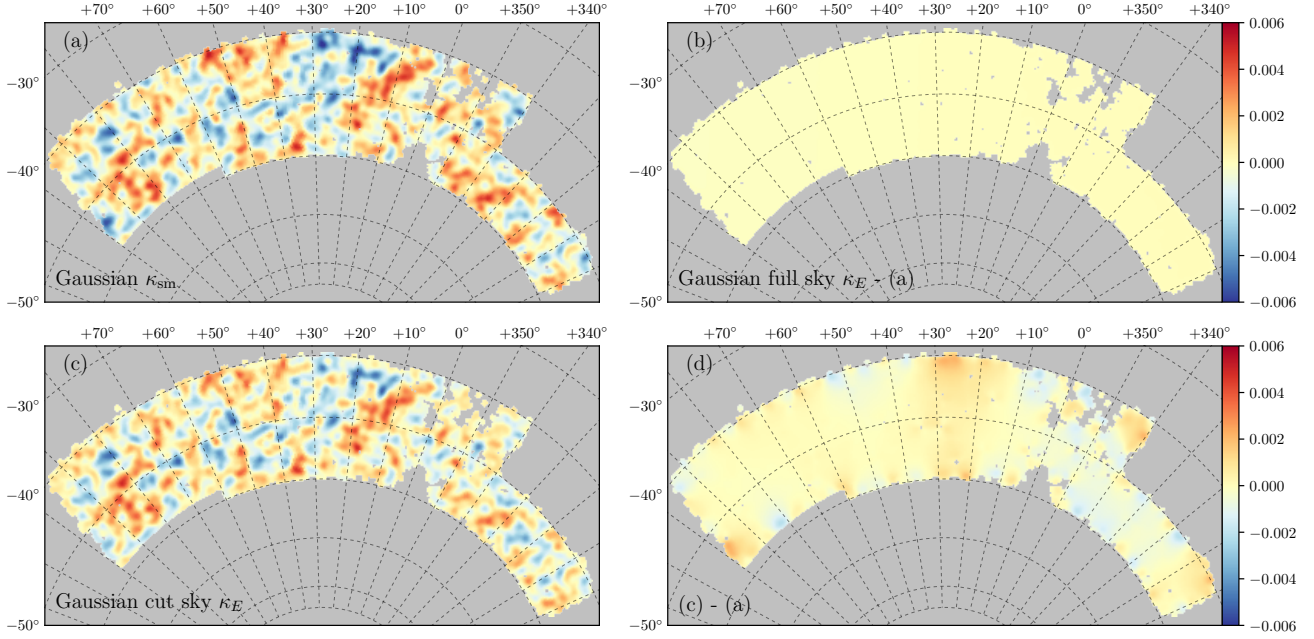
Figure 1. Tests from maps of simulated Gaussian fields. All maps are smoothed with a Gaussian filter of $\sigma_G = 30$ arcminutes, mean-subtracted and projected onto a conic projection. Panel (a) shows the original Gaussian κ_{sm} map; panel (b) is the difference map between the full-sky reconstructed κ_E map and panel (a); panel (c) shows the cut-sky reconstructed κ_E map, and panel (d) shows the difference map between panel (c) and panel (a). The series of maps shows that the reconstruction on the edges is degraded when introducing the mask.

reconstruction using the following statistics:

$$F_1 = \sqrt{\frac{\langle \kappa_E^2 \rangle}{\langle \kappa_{sm}^2 \rangle}}; \; F_2 = \frac{\langle \kappa_E \kappa_{sm} \rangle}{\langle \kappa_{sm}^2 \rangle}, \tag{17}$$

where κ_E is the reconstructed map, κ_{sm} is the true convergence map degraded to the same resolution as κ_E (see Sec. 5.1 for details), $\langle XY \rangle$ is the zero-lag cross-correlation between two maps X and Y, or

$$\langle XY \rangle = \frac{1}{N} \sum_{i=1}^{N} X_i Y_i. \tag{18}$$

The index i runs over all pixels in the map where the pixels are not masked. F_1 is the square-root of the ratio of the second moments of the map. F_2 on the other hand, tests in addition that the phases (in addition to the amplitudes) of the map are reconstructed correctly, or in other words, that the patterns in the maps are correctly reconstructed. F_1 and F_2 are designed to have the same units as κ_E / κ_{sm}. We require that for our final reconstruction (including all noise and systematics effects) of both F_1 and F_2 be consistent with 1 within the 2σ measurement errors. In Appendix B, we perform a subset of the tests above on reconstructing the lensing potential and deflection field described in Sec. 2.

In Sec. 5.3, we take the maps in Sec. 5.2 one step further and examine the PSF of the maps and the second and third moments as a function of smoothing. We require the reconstructed map to have second and third moments consistent with expectation from simulations within 2σ of the measurement errors, which then assures that the reconstruction preserves the distribution of structures on different scales.

We note that the requirements on the reconstruction performance depends on the specific application. Passing the requirements on F_1, F_2 and the moments means that the mean variance, phase, and distribution of power on different scales (on the scales

we tested) in the maps are robust. Extending to further applications would require additional tests.

5.1 Gaussian lensing convergence maps

We consider a set of full-sky, noiseless, Gaussian lensing maps (γ and κ) generated using the HEALPIX routine synfast. These maps are constructed using an input lensing power spectrum for a flat ΛCDM model with cosmological parameters: $\Omega_m = 0.3$, $h = 0.7$, $\Omega_b = 0.047$, $\sigma_8 = 0.82$, $w = -1$. The source redshift distribution $n_s(z)$ is approximately matched to the redshift estimate of BPZ for redshift bin $0.2 < z < 1.3$ in Table 1. We have chosen to demonstrate all the tests on this redshift bin since it contains the highest signal-to-noise. We generate the maps with nside = 1024 and $\ell_{max} = 2 \times$ nside. Note that the ℓ_{max} cut is necessary for further HEALPIX manipulations, since the modes close to the pixel scale can introduce undesired noise. This means that these maps do not contain information on scales beyond ℓ_{max}. The synfast routine outputs three maps that are consistent with the input power spectrum: a spin-0 map and two maps for the two components of the spin-2 field. We can then identify the spin-0 map as the convergence map κ_{sm} and the spin-2 maps as the shear maps γ_{sm}. Since all the lensing maps are effectively smoothed, we use the 'sm' subscript to distinguish these maps (which do not contain information on scales beyond ℓ_{max}) from the true underlying field with infinite resolution. We denote κ_E and κ_B to be the E- and B-mode convergence generated from the smoothed shear maps γ_{sm}.

For visualisation purpose, all maps presented in this paper are first smoothed with a Gaussian filter of $\sigma_G = 30$ arcminutes, then
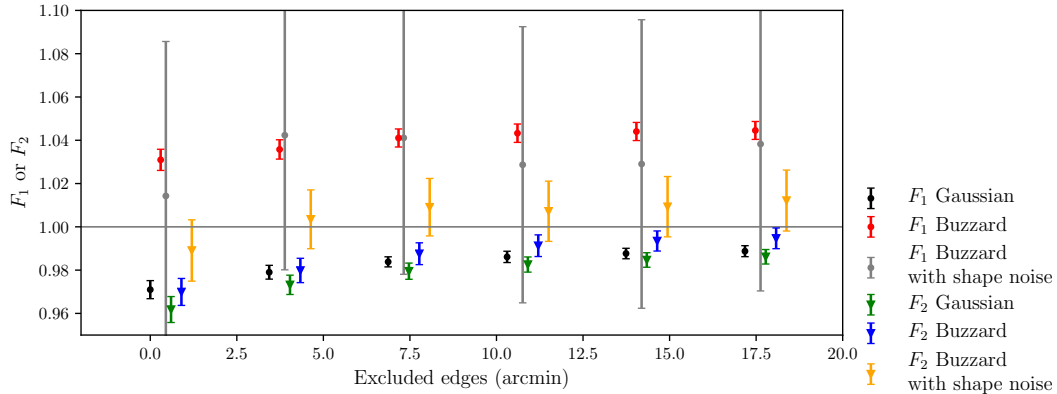
Figure 2. $F_1 = \sqrt{\langle\kappa_E^2\rangle/\langle\kappa_{sm}^2\rangle}$ (circle markers) and $F_2 = \langle\kappa_E\,\kappa_{sm}\rangle/\langle\kappa_{sm}^2\rangle$ (triangle markers) for the reconstructed convergence map from the Gaussian simulations and the Buzzard mock galaxy catalogs. F_1 measures how well the variance of the map is reconstructed, while F_2 measures in addition how well the phase information is reconstructed. $F_1 = F_2 = 1$ means perfect reconstruction. The plot shows how F_1 and F_2 changes when we exclude pixels within a certain distance from the edge of the mask. The larger the exclusion, the less effected the reconstruction is from the edge effects.

mean-subtracted[8], and finally projected onto a plane with Albers equal-area conic using the code SKYMAPPER[9] (for quantitative analyses later we use the raw map themselves). The smoothing scale is chosen so that the highest peaks in the E-mode S/N maps have S/N values greater than ~ 3 and so that one can clearly see the difference between the E and B mode maps. Each of the panels in Fig. 3 are described below:

• Panel (a): noiseless κ_{sm} map directly from `synfast`, cutout in the Y1 footprint.
• Panel (b): subtracting panel (a) from a full-sky, fully sampled, noiseless κ_E reconstruction. This shows that in this ideal situation, the reconstructed κ_E is able to recover κ_{sm} very well with negligible residuals, validating our basic implementation of the shear-to-convergence transformation.
• Panel (c): κ_E reconstruction when applying the Y1 mask to the shear maps. This illustrates overall good reconstruction of the spatial pattern of the maps compared to panel (a). As we have set the mask to zero, the amplitude of the κ_E map is slightly lower than panel (a) at this relatively large smoothing scale.
• Panel (d): subtracting panel (a) from panel (c). We can see edge effects resulting from the Y1 mask, as the pixels on the edge have less information to infer the convergence than the pixels in the centre of the field. In addition, the residuals are small but anti-correlated with the real structure, since the overall amplitude of panel (c) is lower than panel (a).

In Fig. 2 we show in black and green how F_1 and F_2 (Eq. (17)) change when we exclude regions up to 30 arcminutes away from the mask edge. For F_1, we find a value ~ 0.97 when no pixels are excluded and this improves up to about 0.99 when areas 15 arcminutes around the edges are excluded. The fact that $F_1 < 1$ is because we have set the empty pixels to be zero, which dilutes the signal during the reconstruction. We see that F_2 behaves very similar to F_1, which confirms that the reconstruction is good to $\sim 1\%$ in these ideal scenarios with only small effects coming from the dilution due to the edges. We note that the above analysis was evaluated

for the map at $0° <$RA$< 100°$ in order to compare to the Buzzard simulations.

Alternative approaches to dealing with the mask and edge effects include filling in the empty pixels via a smooth interpolation from neighboring pixels and more sophisticated inpainting techniques (Pires et al. 2009). We investigate the former in Appendix A and find that it does not improve the performance of the map reconstruction significantly given the noise level and mask geometry of our data, while the latter is beyond the scope of this paper.

5.2 Convergence maps from simulated galaxy catalogs

Next, we turn to using mock galaxy catalogs generated from N-body simulations. The main differences between these and the Gaussian simulations are that (1) they only sparsely sample the lensing fields at a given thin redshift slice, effectively introducing shot noise, (2) they are derived from a ray-traced lensing field which contains non-Gaussian information, and (3) as discussed in the previous section, the maps naturally contain a small amount of information on scales beyond $\ell_{max} = 2 \times$ nside that we cannot reconstruct when we enforce a ℓ_{max} smoothing during the reconstruction. We would like to understand how these factors affect the reconstruction of the convergence maps. In this section, we mainly use the Buzzard mock galaxy catalogs described in Sec. 3.4 for testing, but we have also tested on an independent set of simulations (the Marenostrum Institut de Ciencies de l'Espai Simulations, or the MICE simulations, Fosalba et al. 2015b,a; Crocce et al. 2015) and found consistent results.

We carry out a series of tests using the convergence map generated for redshift bins that are matched to that used for the data (see Sec. 6). That is, we bin the galaxies using the mean redshift reported by the photo-z code and check that the resulting $n(z)$ reported by BPZ is close to that of our data. Next, we make three maps using directly the quantities provided by the simulation:

• κ_{pix}: convergence
• γ_{pix}: shear
• ε_{pix}: galaxy shapes.

These maps are constructed with the same resolution (nside = 1024) as before. The subscript 'pix' denotes pixelised quantities. Next, we generate several other versions of convergence maps.

---

[8] Since lensing reconstruction is only valid up to a constant offset, we subtract the mean to avoid this constant additive bias.
[9] https://github.com/pmelchior/skymapper
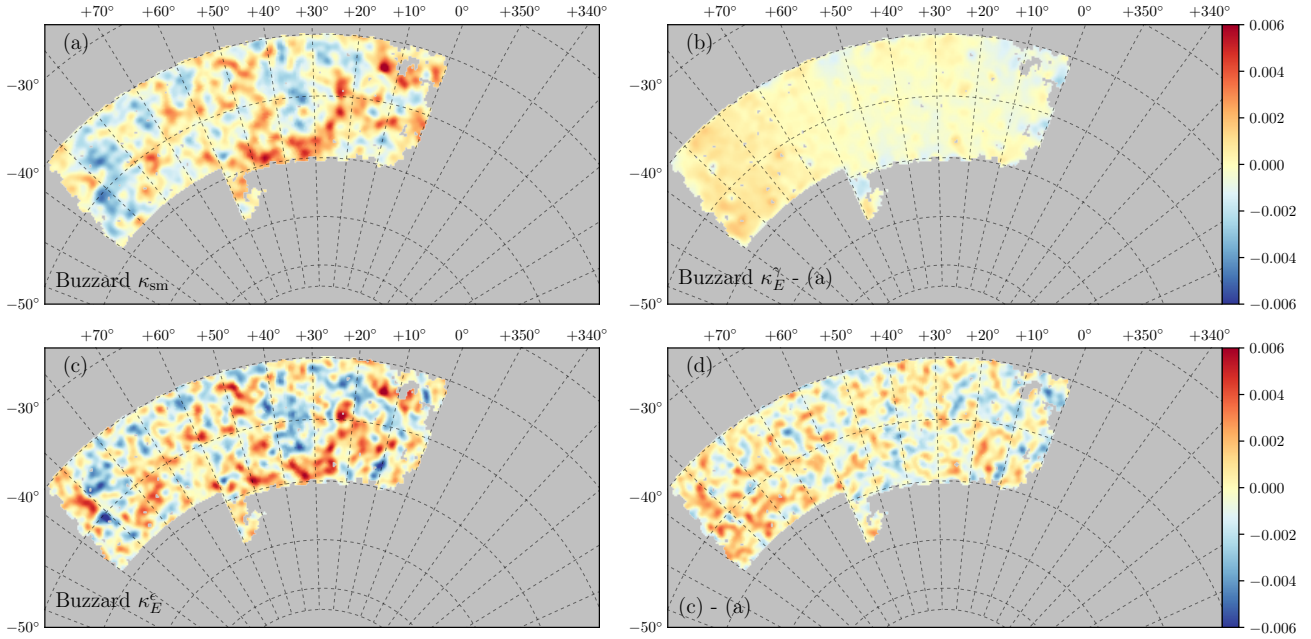
Figure 3. This figure is similar to Fig. 1 but using the Buzzard mock galaxy simulations. Panel (a) shows the original Buzzard κ_{sm} map; panel (b) shows the difference between the reconstructed κ_E^γ map (without shape noise) and panel (a); panel (c) shows the reconstructed κ_E^ε map (with shape noise), and panel (d) shows the difference map between panel (c) and panel (a).

- κ_{sm}: to ensure that all maps we compare later have the same resolution, we smooth the κ_{pix} map by removing all ℓ modes beyond $\ell_{max} = 2 \times$ nside;
- κ_E^γ, κ_B^γ: E- and B-mode convergence constructed using shear γ_{pix};
- κ_E^ε, κ_B^ε: E- and B-mode convergence constructed using galaxy shapes ε_{pix}.

In Fig. 3 we compare visually several of these reconstructed maps:

- Panel (a): κ_{sm} map from the Buzzard simulation. Comparing with panel (a) of Fig. 1, one can see that the convergence map from the galaxy catalog has similar amplitudes and characteristic spatial patterns as the Gaussian map. The Buzzard maps appear slightly more clustered, which comes from the non-Gaussian nature of these maps compared to the pure Gaussian simulations.
- Panel (b): subtracting panel (a) from the reconstructed κ_E^γ map from Buzzard, which includes shot noise from the finite sampling from the galaxies and the Y1 mask but no shape noise. Similar to panel (d) of Fig. 1, there is an anti-correlation of the low-level residuals with the true structures.
- Panel (c): reconstructed κ_E^ε map from the Buzzard simulation, which includes shot noise from the finite sampling from the galaxies, the Y1 mask and shape noise. We find the amplitude of the map to be higher than the κ_{sm} map in panel (a) and that there are spurious structures that arise from noise which do not correspond to real structures in the κ_{sm} map. However, the resemblance of the κ_E^ε map to the κ_{sm} map is still very obvious, especially the large-scale patterns in the maps. This suggests that despite of noise, the majority of the structures in the κ_E^ε map are associated with real structures on this smoothing scale.
- Panel (d): subtracting panel (a) from panel (c). We see more clearly the shape noise-induced small-scale noise peaks as well as a large scale pattern that is very similar to that in panel (b). The

edge effect, in comparison, becomes less visible in the presence of shape noise.

In Fig. 2 we again show the F_1 (red) and F_2 (blue) statistics as a function of the area excluded around the mask. We find that F_2 behaves very similar to the Gaussian version shown in green, while F_1 appears systematically higher than the Gaussian simulations. This indicates that the reconstruction with the mock galaxy catalogs introduces un-correlated noise in κ_E, causing the overall variance in the map to be larger, while the phase remains the same. This additional noise comes from the finite sampling of the shear field inside each pixel — the mean shear over all galaxies inside each pixel is different from the true mean shear in that pixel. This noise can be suppressed by smoothing the maps at a scale slightly larger than the pixel scale, as can be seen in Fig. 4. Both F_1 and F_2 increase by a few percent when excluding the edges. When introducing shape noise, the error bars on F_2 increase, but the amplitude stays roughly unchanged, suggesting that on average, shape noise does not change the phase information. The raw F_1 with shape noise is will be dominated by shape noise in the denominator, therefore we show instead the "de-noised" version F_1 defined as $\sqrt{(\langle \kappa_E^2 \rangle - \langle \kappa_{E,ran}^2 \rangle)/\langle \kappa_{sm}^2 \rangle}$, where $\kappa_{E,ran}$ is a convergence map constructed by randomizing the ellipticities. In the remaining of the paper, "F_1 with shape noise" refers to this de-noised quantity.

Overall, we find that at the number density and pixel resolution of this particular map ($0.2 < z < 1.3$), the performance of the reconstruction from the galaxy catalog is similar to that from the Gaussian map in terms of the effect of masking, though the reconstruction is noisier for the galaxy catalogs which results in a higher F_1. After including shape noise, both F_1 and F_2 are consistent with 1 even without exclusion of the edge pixels. We also note that if we perform the same tests on a different redshift bin where the number density of galaxies is lower, the performance of the reconstruction using both the Gaussian and the Buzzard simulations becomes
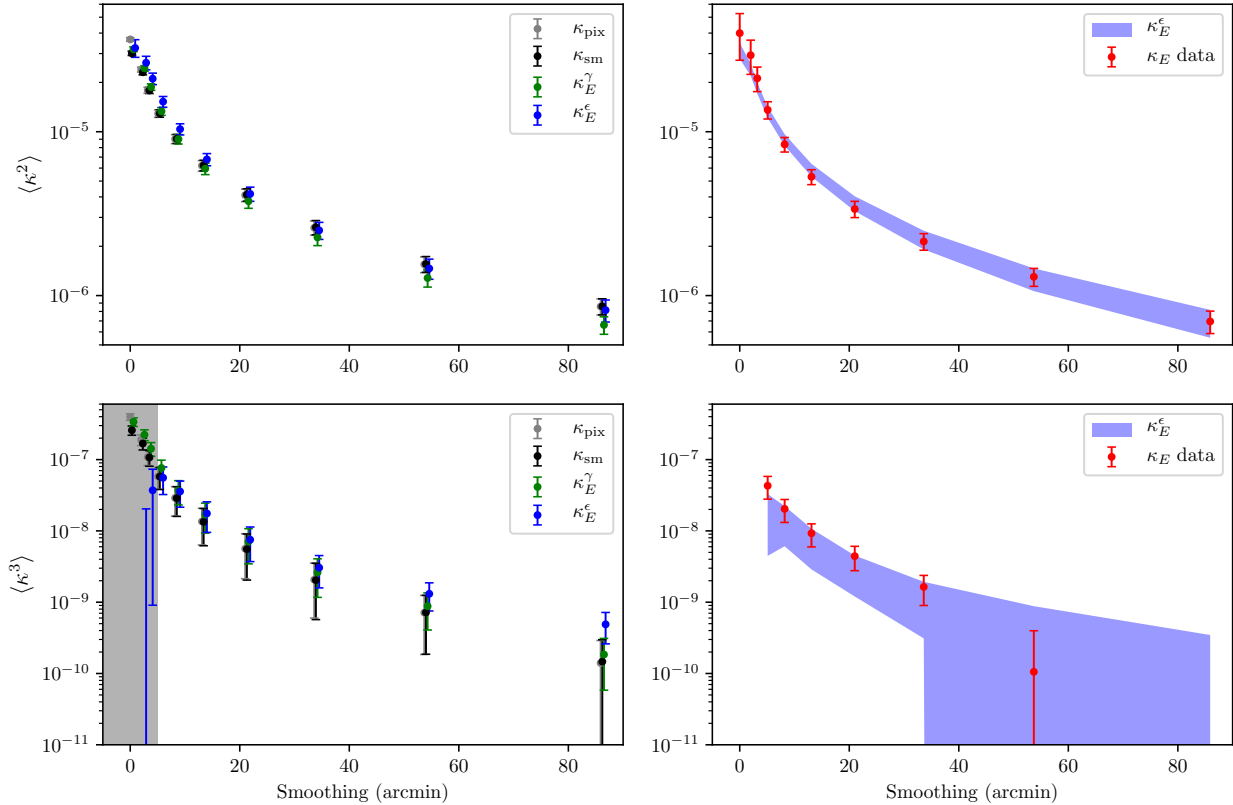
Figure 4. The upper left panel shows the second moments of the maps as a function of smoothing scale for different κ maps in one Buzzard simulation, from the most idealised noiseless case (grey), to two intermediate stages (black and green), and to the κ_E^ε map that includes observational noise that match to the data (blue). The shaded blue band in the upper right panel shows the mean and standard deviation of the κ_E^ε measurement for 12 independent Buzzard realisations. The measurement from the data is shown in red. The lower panels show the same as the upper panels, except for the third moments. The grey band in the lower left panel marks the scales that we remove for third moments analyses due to noise on small scales. All maps are generated for the redshift bin $0.2 < z < 1.3$.

worse with the same pixel resolution. That is, the three factors — resolution of the map, effect of the edges, and number density of the source galaxies — are tightly coupled. If the chosen pixel resolution is sub-optimal for the data set, the reconstruction could be significantly biased. For example, if the pixel size is much smaller than the typical separation of source galaxies, there will be a large number of empty pixels, which would result in a lower amplitude in the reconstructed maps. For our sample of the DES Y1 shear catalog, we perform quantitative studies only on the highest S/N map at $0.2 < z < 1.3$ with the pixel scale of 3.44 arcminutes. We test the F_1 and F_2 statistics for this map in different resolutions and find that increasing or decreasing the resolution by a factor of 2 in the noiseless Buzzard simulation changes F_1 and F_2 by at most 3%.

5.3 Moments and PDF

One final powerful test of the reconstruction is to look at the moments and the PDF of the maps. In this section, we examine the second and third moments of the various maps used in Sec. 5.2 as we progressively smooth the maps on increasingly larger scales. Since these moments of the convergence maps as a function of smoothing scale are sensitive to cosmology (Bernardeau et al. 1997; Jain & Seljak 1997; Jain & Van Waerbeke 2000), it is important to verify how well the reconstructed maps preserve these characteristics. A similar test was performed in Van Waerbeke et al. (2013),

where they checked up to the 5th moment of the maps. We only consider the second and the third moments as the galaxy number density in our maps is lower compared to that used in Van Waerbeke et al. (2013), and the higher moments are more sensitive to the noise in the maps. We begin with the set of Buzzard maps described in the previous section: κ_{pix}, κ_{sm}, κ_E^γ and κ_E^ε. For each map, we smooth with a Gaussian filter with $\sigma_G = [0.0, 2., 3.2, 5.1, 8.2, 13.1, 21.0, 33.6, 53.7, 85.9]$ arcminutes, where the first case is equivalent to the unsmoothed map examined previously. To correct for the effect of smoothing on the edge pixels, we smooth the mask with the same filter and dividing the map by the smoothed mask. We then calculate the second moment $\langle \kappa^2 \rangle$ and third moments $\langle \kappa^3 \rangle$ of these maps for the different smoothing scales. For κ_E^ε, we follow the de-noising prescription described in Van Waerbeke et al. (2013). That is

$$\langle (\kappa_{E,\mathrm{denoise}}^\varepsilon)^2 \rangle = \langle (\kappa_E^\varepsilon)^2 \rangle - \langle (\kappa_{E,\mathrm{ran}}^\varepsilon)^2 \rangle, \tag{19}$$

where $\kappa_{E,\mathrm{ran}}^\varepsilon$ is obtained from shuffling the positions of the galaxies while keeping their ellipticities fixed. $\kappa_{E,\mathrm{ran}}^\varepsilon$ is a measure of the contribution from shape noise to the second moments and thus needs to be subtracted from the raw measured second moments.

The second and third moments of the various κ maps as a function of smoothing scale are shown in the left panels of Fig. 4. The error bars are estimated via the standard Jackknife approach. We find that κ_{pix} and κ_{sm} disagree slightly with no smoothing, but once a small amount of smoothing is applied, which removes the
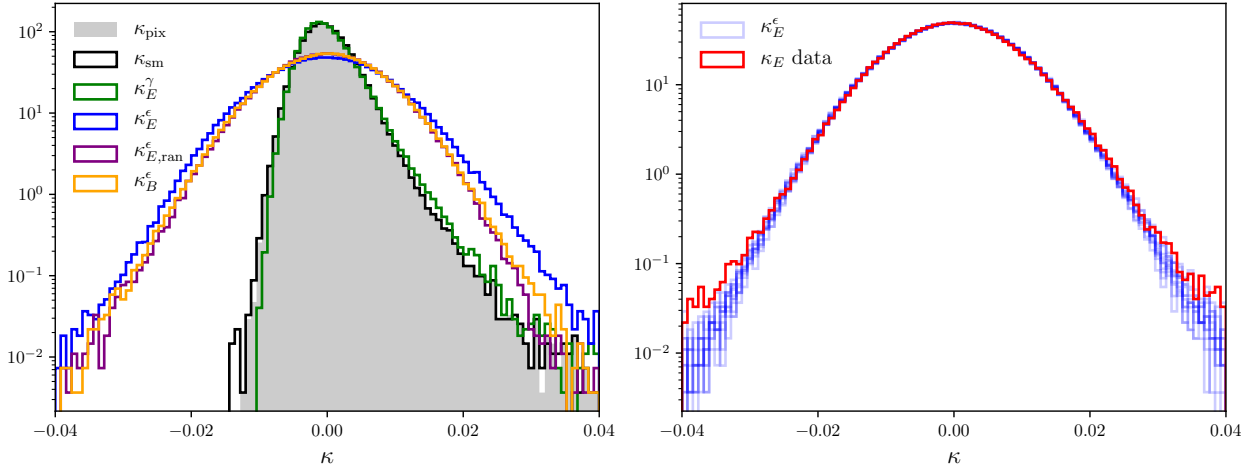
Figure 5. Pixel histograms for various maps in simulation and data when smoothed with a Gaussian filter of $\sigma_G = 5.1$ arcminutes. The left panel shows the pixel histograms for maps generated from one Buzzard simulation going from the most ideal noiseless scenario (grey) to two intermediate stages (black and green), to the final simulation with noise properties matched to the data (blue). Also shown are the histogram for the random map (purple), which is consistent with the B-mode map (orange). The faint blue lines in the right panel shows the histograms for κ_E^ε in 12 independent Buzzard realisations, while the red line shows the pixel histogram for the data κ_E map (See Section 6.1 for discussion). All maps are generated for the redshift bin $0.2 < z < 1.3$.

very small scale information in the $\kappa_{\rm pix}$ map, they agree vey well. $\kappa_{\rm sm}$ and κ_E^γ are also consistent within the error bars, suggesting that the reconstruction does not distort the information about how the structures of different scales are distributed in the maps. Finally, κ_E^γ and κ_E^ε agree with each other within 1σ for the second moments on all scales and for the third moments on scales > 5 arcminutes. The error bars for κ_E^ε are larger due to shape noise. We note that the third moment measurements on small scales are not recovered due to the noise on small scales (for a shear signal of 1%, a smoothing scale of 5 arcminutes would result in an effective S/N of ~ 0.5). We therefore remove scales smaller than 5 arcminutes in further analyses on the third moments. We also find that on scales > 40 arcminutes, noise can cause the third moments to be negative. We repeat the measurement for 12 independent realisations of the Buzzard simulations. The mean and standard deviation of the 12 measurements for κ_E^ε are shown in the right panels of Fig. 4. This provides a measure of the contribution from cosmic variance. We find that, within the uncertainties from the measurement and cosmic variance, we can indeed recover the second and third moments as a function of smoothing scales with our reconstruction method for scale larger than 5 arcminutes in the map corresponding to $0.2 < z < 1.3$. The data point for the third moment on the largest scale is $(-2.9\pm1.6)\times10^{-10}$, which is not shown on the log plot, but is consistent within 2σ with the simulation value of $(0.97\pm2.5)\times10^{-10}$.

It is also instructive to look at the PDF of the different maps for one smoothing scale in Fig. 4. The left panel of Fig. 5 shows the distribution of $\kappa_{\rm pix}$ (grey shaded), $\kappa_{\rm sm}$ (black) and κ_E^γ (green) when smoothed by a Gaussian filter of 5.1 arcminutes. We find that the three histograms agree very well, and the non-Gaussian nature of the PDF is apparent. These distributions closely resemble the log-normal distribution and is consistent with the results shown in Clerkin et al. (2015). The distribution of κ_E^ε (blue), κ_B^ε (orange) and $\kappa_{E,\rm ran}^\varepsilon$ (purple) are also shown. Due to the added shape noise, these three fields appear much more Gaussian and the shape of the PDF is much broader. The fact that the distribution of $\kappa_{E,\rm ran}^\varepsilon$ is consistent with κ_B^ε suggests that shape noise is the main contributor of the B-

mode map on these smoothing scales, rather than B-mode leakage due to imperfect reconstruction. We also check by looking at the B-mode signal in the noiseless reconstruction scenario, and find it to be negligible compared to the B-mode from shape noise. The shape of the of κ_E^ε PDF is qualitatively different from $\kappa_{E,\rm ran}^\varepsilon$ and κ_B^ε — the κ_E^ε map contains more extreme high and low values, which correspond to real peaks and voids in the mass distribution. The κ_E^ε PDF is also slightly skewed towards positive values, which is the imprint of the skewed true κ distribution seem in $\kappa_{\rm pix}$.

6 DES Y1 WEAK LENSING MAPS

6.1 Convergence maps

Now we present the main goal of the paper. In Fig. 6 we show the signal-to-noise (S/N) maps associated with the E-mode and B-mode convergence generated from the METACALIBRATION catalog for galaxies in the redshift range $0.2 < z < 1.3$ and smoothed with $\sigma_G = 30$ arcminutes. The S/N in these maps apply both to the positive (peaks) and negative (voids) values — extreme positive and negative values are significant, while values close to zero are more likely to be consistent with noise. In Fig. 7, maps for the four tomographic bins are shown. The IM3SHAPE convergence maps in all the redshift bins are shown in Appendix C for comparison, together with maps generated using the Science Verification data (Vikram et al. 2015; Chang et al. 2015).

We first look at the E-mode maps. Fig. 6 includes the full redshift range $(0.2 < z < 1.3)$ and thus has much higher signal-to-noise compared to the tomographic maps in Fig. 7, as expected from the higher number density of source galaxies. The visual impression of the map is very similar to the maps generated from the mock galaxy catalogs shown in Fig. 3, where there is an imprint of large-scale structure stretched over tens of degrees. The area close to RA$\sim 0°$ suffers from a more complicated mask structure as well as shallower depth, which results in a lower S/N in the map in that region. In Fig. 7, we find that the redshift bin $0.63 < z < 0.9$ has the highest S/N, which is due to both the higher signal at higher redshift and
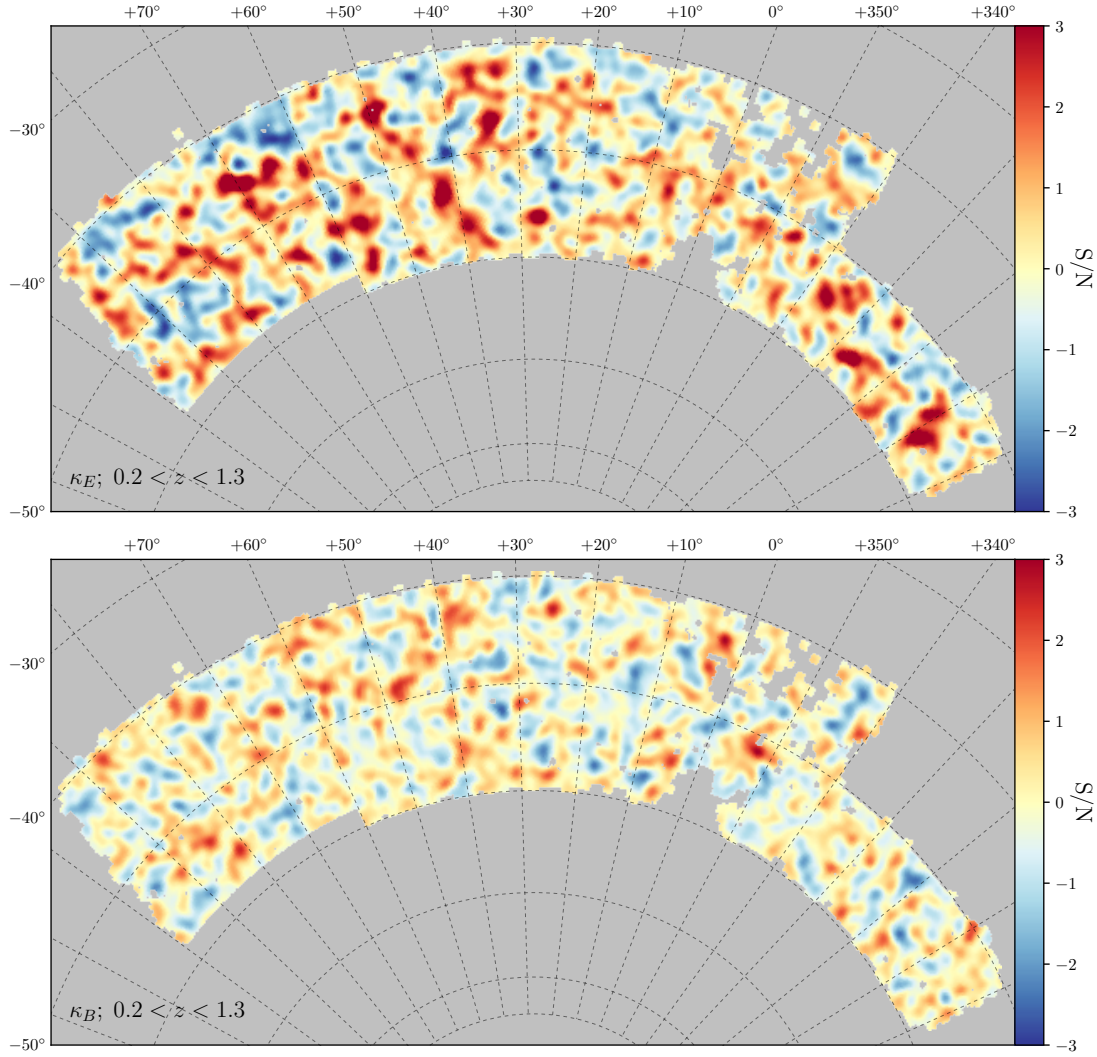
Figure 6. Pixel signal-to-noise (S/N) $\kappa_E/\sigma(\kappa_E)$ maps (top) and $\kappa_B/\sigma(\kappa_B)$ maps (bottom) constructed from the METACALIBRATION catalog for galaxies in the redshift range of $0.2 < z < 1.3$, smoothed by a Gaussian filter of $\sigma_G = 30$ arcminutes. $\sigma(\kappa_E)$ and $\sigma(\kappa_B)$ are estimated by Eq. (16).

the lower noise coming from the higher number density of source galaxies. Structures that show up in a given map are likely to also show up in the neighbouring redshift bins, since the mass that is contributing to the lensing in one map is likely to also lens galaxies in neighbouring redshift bins. This is apparent in e.g. the structures at (RA, Dec)=(35°, -48°) and (58°, -55°). Next, we compare the E-mode maps with their B-mode counterpart in Fig. 6 and Fig. 7. In general, the B-mode maps have lower overall amplitudes. The mean absolute S/N of the E-mode map is ~1.5 times larger than the B-mode map at this smoothing scale. For a smoothing scale of $\sigma_G =80$ arcminutes, this ratio increases to ~ 2. There are no significant correlations between the E- and the B-mode maps in Fig. 6 and Fig. 7: we find that the Pearson correlation coefficients[10] are all consistent with zero, as expected for maps where systematic effects are not dominant. Comparing the four tomographic B-mode maps

in Fig. 7, there is no obvious correlation between the structures in one map with maps of neighbouring redshift bins. We find that the Pearson correlation coefficient between the second and third (third and fourth) redshift bins for the B-mode maps is 8 (5.5) times lower than that for the E-mode maps. The E and B-mode maps for the lowest redshift bin $0.2 < z < 0.43$ have similar levels of S/N, which is expected since the lensing signal at low redshift is weak and the noise level is high.

We now examine the second and third moments of the κ_E maps similar to the tests in Sec. 5.2. For direct comparison with simulations, the measurements are done using the map with the full redshift range $0.2 < z < 1.3$ and in the region of $0° <$RA$< 100°$. Our results are shown in the right panels of Fig. 4, where the mean and standard deviation of the 12 noisy simulation results are also overlaid.

We note that we do not expect perfect agreement between the simulation and data for several reasons: first, the detailed shape noise incorporated in the simulations is only an approximation to the METACALIBRATION shape noise. In particular, there is no correlation of the shape noise with other galaxy properties in our sim-

---

[10] The Pearson correlation coefficient two maps X and Y is defined as $\langle(X - \bar{X})(Y - \bar{Y})\rangle/(\sigma_X \sigma_Y)$, where $\bar{X}$ and $\bar{Y}$ are the mean pixel values for the two maps, the $\langle\rangle$ averages over all pixels in the map, and σ indicates the standard deviation of the pixel values in each map.
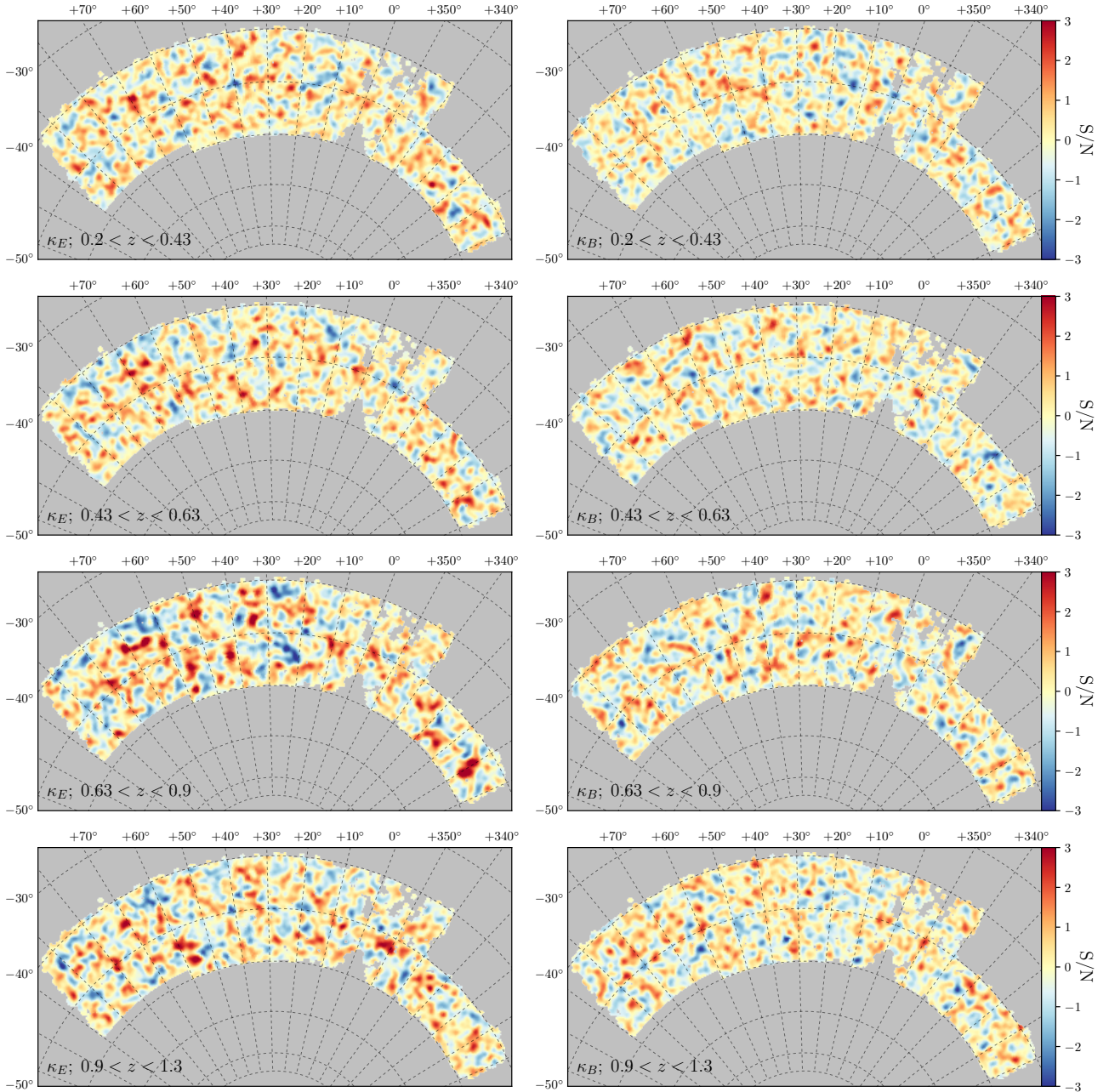
Figure 7. Same as Fig. 6 but for the four tomographic maps. The $\kappa_E/\sigma(\kappa_E)$ maps are shown on the left and the $\kappa_B/\sigma(\kappa_B)$ maps are shown on the right.

ulations. This, however, should be a second-order effect, since we do not expect the galaxy properties to correlate with the true convergence. Second, the number density and $n(z)$ in the simulations only approximately match the data as we discussed in Sec. 3.4. This is also a second-order effect since lensing is mainly sensitive to the mean redshift of the lensing kernel. The detailed shape of the $n(z)$ will not significantly alter the convergence maps. Finally, the simulations assume a certain cosmology that may not be the true one. As $\langle\kappa^2\rangle \propto \sigma_8^2\Omega_m^{1.5}$ and $\langle\kappa^3\rangle/\langle\kappa^2\rangle^2 \propto \sigma_8^{-0.8}$ (Bernardeau et al. 1997; Jain & Van Waerbeke 2000), these measurements are directly sensitive to the cosmological parameters. Given the current constraints in σ_8 and Ω_m from Planck Collaboration et al. (2016),

changing the cosmological parameters by 2σ does not affect the comparison carried out here.

From Fig. 4, we find very good agreement between the measurements from data and simulations in the overall amplitude and trend of the second and third moments as a function of smoothing scale. The fact that our measurements are in agreement with the simulations suggests that they are also in agreement with the cosmology assumed in the simulations (see Sec. 3.4), though the error bars are fairly large compared to e.g. Troxel et al. (2017); DES Collaboration et al. (2017). The histograms of the κ_E and κ_B maps smoothed with a 5.1 arcminute Gaussian filter are shown in the right panel of Fig. 5, together with the simulation counterparts generated from the 12 Buzzard simulations. Again, we find good
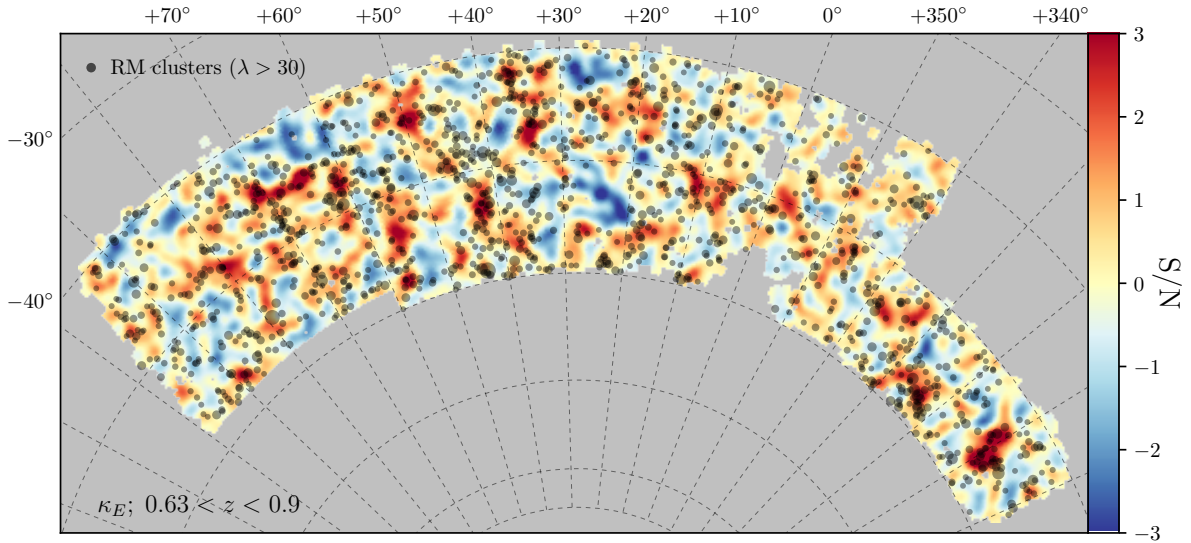
Figure 8. Top panel shows the κ_E map at $0.63 < z < 0.9$, overlaid with REDMAPPER (RM) clusters at $\lambda > 30$ and $0.2 < z < 0.5$ (black solid circles). The size of the circles scale linearly with λ, or the cluster mass.

agreement in the shape and width of the κ_E PDF between the simulation and the data. The slightly narrower width of the simulation PDF at the extreme κ_E values is likely due to the lack of spatial variation of shape noise, which is not properly incorporated in the simulations.

Finally, as an additional visual inspection, we overlay a sample of REDMAPPER galaxy clusters (Rykoff et al. 2016) onto the E-mode map at $0.63 < z < 0.9$ as shown in Fig. 8. The galaxy clusters are selected to be in the redshift range $0.2 < z < 0.5$ (roughly the peak of the lensing efficiency of the map) and the richness range $\lambda > 30$ (corresponding to roughly a mass greater than 2×10^{14} M$_\odot$; Melchior et al. 2017). Each circle indicates a cluster, with the size of the circle proportion to the richness (mass) of the cluster. Visually we can see the correlation between the cluster positions and the region of the map with high κ values. It is noticeable that the high κ regions in the map are often associated with an ensemble of smaller clusters rather than one large cluster, while there is a clear lack of clusters inside most of the "void" regions in the map. There are exceptions, though, where very high S/N peaks do not line up with the cluster distributions. For example, the peaks at (RA, Dec)=(55.9°, -53.8°) and (34.3°, -47.5°) do not correspond to any clusters at the centre of the peak, and the void area around (RA, Dec)=(60.3°,-43.3°) overlaps with several clusters. This could be in part due to the shape noise moving the locations of peaks and voids, as we have seen in Fig. 3. Nevertheless, further investigation of these structures would be interesting in identifying e.g. massive structures with relatively low luminosity. Overall, in Fig. 8 we find that there are ~30% of clusters in pixels above S/N>1, and ~6.5% in pixels S/N<-1; ~13% of clusters in pixels above S/N>2, and none in pixels S/N<-2.

6.2 Systematic tests

We have explored, in Sec. 5, the systematic effects associated with the reconstruction algorithm, masking, shot noise, and shape noise using simulations. We also examined the zeroth order systematic effects in the data by looking at the B mode convergence maps in Sec. 6.1. In this section we concentrate on examining other poten-

tial sources of systematic effects that could contaminate our maps. Specifically, we look at whether there exists any spurious correlation between our maps and quantities that are not expected to correlate with the convergence maps. This technique is similar to that used in Elvin-Poole et al. (2017).

We first identify a number of potential systematics that could contaminate the κ_E maps. The potential systematics presented here are listed below:

- κ_B: B-mode convergence map
- ε^1, ε^2: the mean galaxy ellipticity
- ε^1_{PSF}, ε^2_{PSF}: the mean PSF ellipticity
- $\kappa_{E,PSF}$, $\kappa_{B,PSF}$: κ_E and κ_B maps generated from ε^1_{PSF} and ε^2_{PSF}
- R_{PSF}: the mean PSF size used for galaxy shape measurement[11]
- $R_{PSF,r}$: the mean r-band PSF FWHM size
- depth$_r$: the mean r-band magnitude limit[12]
- airmass$_r$: the mean r-band airmass.

Note that we have checked the PSF size, depth and airmass quantities for other filter bands but only present here the r-band quantities. For potential systematics s, we construct map M^s. For quantities where we expect the mean to be close to zero ($\kappa_B, \varepsilon^1, \varepsilon^2, \varepsilon^1_{PSF}, \varepsilon^2_{PSF}, \kappa_{E,PSF}, \kappa_{B,PSF}$), M^s is constructed using the mean-subtracted values; whereas for the rest of the quantities where the mean is non-zero, we use the fractional contrast of the map $M^s = \delta_s = \frac{s - \bar{s}}{\bar{s}}$.

We first look for correlation at the pixel level between the four tomographic κ_E maps with each of the above potential systematics s. That is, we are interested in whether the high κ_E values are associated with a certain systematic quantity being high or low. To do this, we bin the pixels in the systematics templates into 10 bins depending on the value of the pixels, and measure the average convergence in the pixels assigned to each of the 10 bins. The error bars are evaluated using a Jackknife approach. We then perform a
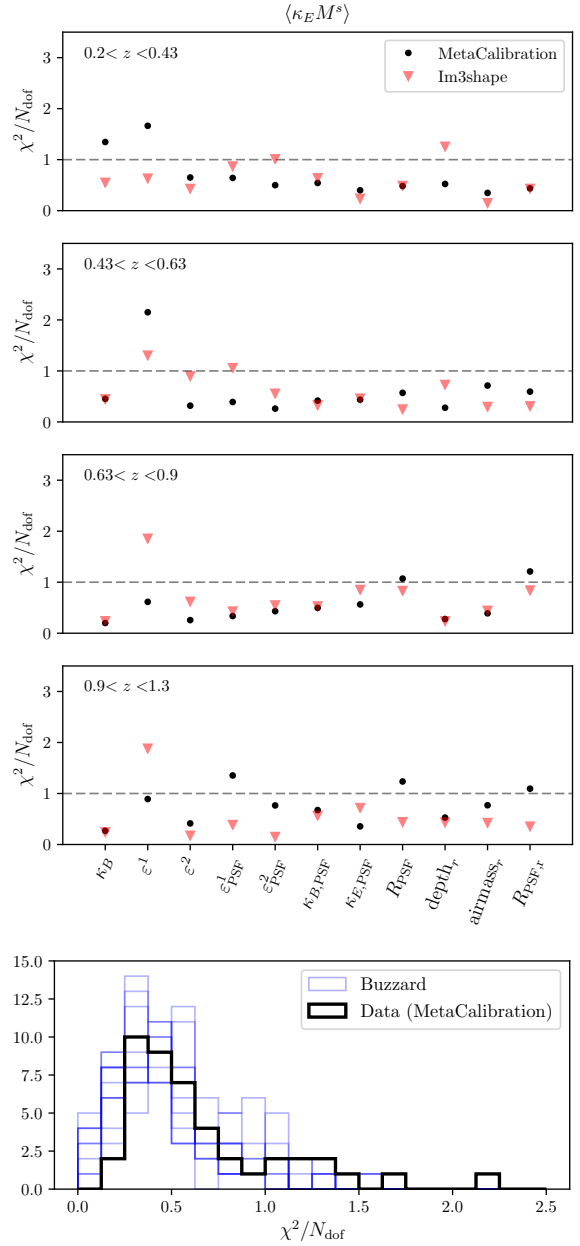
---

[11] We use the quantity `mean_psf_fwhm` in the IM3SHAPE catalog and `psfrec_T` in the METACALIBRATION catalog.
[12] These are 10σ detection limits for galaxies.
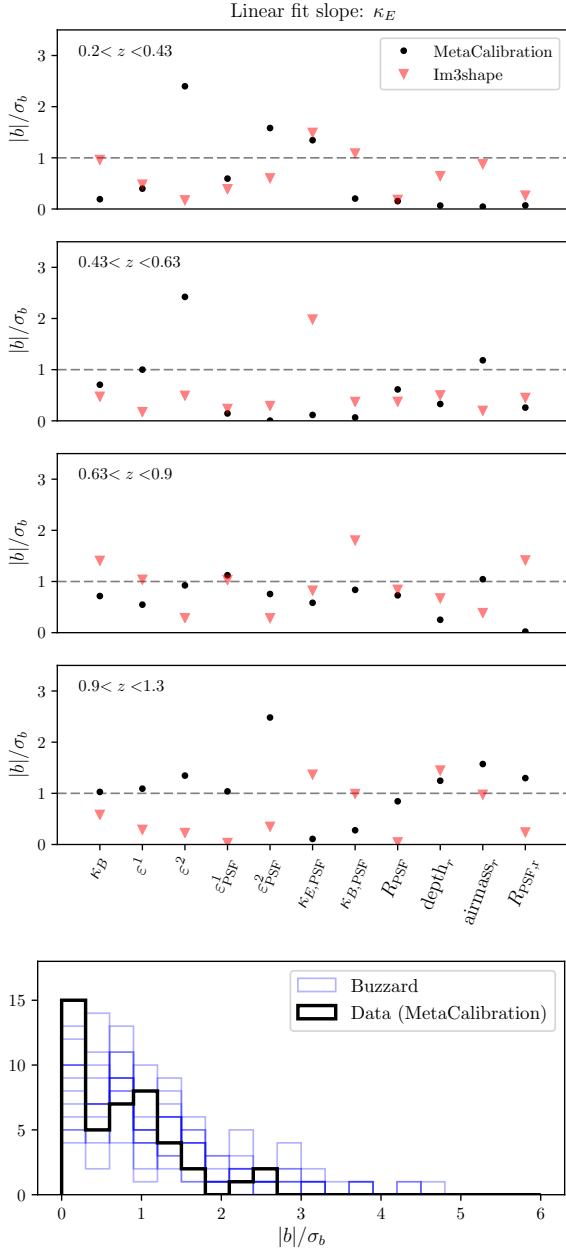
Figure 9. The upper four panels show the absolute value of the best-fit slope b divided by the uncertainty of b for the linear fit of κ_E vs. various systematics templates. $|b|/\sigma_b$ measures the significance of a trend between the convergence and the systematics templates. The four panels correspond to the four tomographic bins which we construct the κ_E maps, and the two set of points correspond to the two shear catalogs. The list of systematics templates are labeled for the last redshift bin. The bottom panel shows a histogram of $|b|/\sigma(b)$ measured from the 12 Buzzard simulations (thin blue lines) compared to METACALIBRATION data points (thick black line).

Figure 10. Similar to Fig. 9, the upper four panels show the reduced χ^2 for the cross-correlation of the κ_E maps with various systematics templates to be consistent with zero. The cross-correlation is measured for a range of scales, with a total of 8 data points, thus the number of degrees-of-freedom ($N_{\rm dof}$) for the χ^2 is 8. The bottom panel shows a histogram of the reduced χ^2 measured from the 12 Buzzard simulations (thin blue lines) compared to METACALIBRATION data points (thick black line).

linear fit with intercept a and slope b to the measurements. In order to see whether there is a significant correlation between the value of the convergence and the value of the systematics template, we plot $|b|/\sigma_b$ in Fig. 9. There is one data point that has a $|b|/\sigma_b$ value larger than 3 ($\kappa_{E,\rm PSF}$ for METACALIBRATION in highest redshift bin), which we show in the histogram in the bottom panel. To understand whether these $|b|/\sigma_b$ values are a cause of concern, we perform the same analysis for the 12 Buzzard simulation maps by

cross-correlating them with the systematics templates. Since these simulations cannot be possibly correlated with the data, this measurement provides a quantitative way to interpret the results. The distribution of all $|b|/\sigma_b$ values are shown in the bottom panel of Fig. 9, together with the METACALIBRATION results (as the simulations are matched to the characteristics of the METACALIBRATION catalog). We find that 97% (88%) of the points in the simulations are below 3σ (2σ), which is in reasonable agreement with that from the data (98% of the points below 3σ and 91% of the

points below 2σ). The overall distribution of $|b|/\sigma_b$ values in the simulations also agrees well with the data.

Next, we compute the two-point angular cross correlation between the convergence maps and the systematics templates. This measurement tests the potential contamination of cross-correlating the κ maps with other maps, such as that investigated in Sec. 7.1. We measure

$$\langle \kappa M^s \rangle (\theta_i) = \frac{1}{N_i} \sum_j^{N_i} (\kappa M^s)_j, \quad (20)$$

where M^s is the systematics template of interest and the sum is over all pairs of pixels j in the maps separated by angular distance within the bin θ_i. The correlation function is evaluated in 8 logarithmically separated angular bins θ_i between 10 and 200 arcminutes. The covariance matrix is derived from the Jackknife approach. We then calculate the reduced χ^2 of each correlation for it to be consistent with null signal, ie. $\langle \kappa M^s \rangle (\theta_i) = 0$, at all θ_i, where the χ^2 is defined through

$$\chi^2 = D Cov_D^{-1} D^T \quad (21)$$

where $D = \langle \kappa M^s \rangle (\theta_i)$ is the angular correlation function and Cov_D is the covariance matrix between the 8 angular bins.

The results of the two-point cross-correlation are shown in Fig. 10. We also perform similar measurements using the 12 Buzzard simulations and show the total distribution of the reduced χ^2 in the bottom panel. We find that reduced χ^2 for all combinations of maps, shear catalogs, and redshift bins, all fall below 3, indicating no significant contamination in the maps directly introduced by these potential systematics quantities on the two-point level. Comparing with simulations also shows that the overall distribution of these reduced χ^2 values are consistent with no correlation between the κ_E maps and the systematics templates. We find that 100% (92%) of the points in the simulations are below 2σ (1σ), which is in reasonable agreement with that from the data (98% of the points below 2σ and 80% of the points below 1σ).

7   APPLICATIONS OF DES Y1 MASS MAP

In this section we present two applications of the convergence map constructed from this work. In Sec. 7.1 we cross-correlate the convergence maps with foreground mass tracers to demonstrate that our maps do indeed contain significant signal and is consistent with expectation. In Sec. 7.2 we take a closer look at some of the high signal-to-noise structure in the maps and discuss the physical interpretation for the largest peaks and voids respectively. We defer some of the more involved applications (e.g. cross-correlation of the convergence maps to CMB lensing maps, peak statistics) to future work.

7.1   Cross correlation of mass and light

One of the motivations for generating a convergence map instead of using the weak lensing shear directly is that in many cases a scalar field is easier to manipulate and cross-correlate with other data sets compared to a spin-2 field. Here we demonstrate some of the usages by cross-correlating the convergence maps in Fig. 7 with other tracers of mass. Specifically, we look at a flux-limited galaxy sample (described in Sec. 3.3) and the REDMAGIC Luminous Red Galaxies (LRG) sample (Rykoff et al. 2016). The amplitudes of these cross-correlations will be a direct measure of the galaxy bias for the different samples (see e.g. Pujol et al. 2016;

Chang et al. 2016). Note that the cross-correlation can naturally extend to include maps of other wavelengths such as X-ray, Gamma ray (Shirasaki et al. 2014), H$_I$ neutral hydrogen (Kirk et al. 2015), the CMB, CMB lensing (Liu & Hill 2015; Hand et al. 2015; Kirk et al. 2016) and others.

In this analysis, we opt for calculating the real-space 2-point correlation function similar to that used in Sec. 6.2,

$$\langle \kappa \delta^X \rangle (\theta_i) = \frac{1}{N_i} \sum_j^{N_i} (\kappa \delta^X)_j, \quad (22)$$

where X denotes the specific sample of interest (flux-limited galaxy sample or REDMAGIC galaxies in different redshift ranges). $\delta = \frac{n - \bar{n}}{\bar{n}}$ is the density contrast of the sample, where n is the number of counts per pixel and $\bar{n}$ is the mean number count over the full map. The average is calculated for all pairs of points j whose angular separation θ fall in the angular bin θ_i. The cross-correlation is calculated for scales 2.5 to 250 arcminutes. In later analyses where we compare the cross-correlation between the convergence map and the two foreground samples, we exclude scales larger than 100 arcminutes and smaller than 15 arcminutes. The small-scale cutoff corresponds to about 3 times the scale corresponding to ℓ_{max}, while the large-scale cutoff corresponds to the size of the Jackknife region.

We begin with testing whether the cross-correlation between the κ_E and κ_B map with a foreground flux-limited galaxy sample is consistent with expectation from the simulations. We use the same set of mock galaxy catalogs used in Sec. 5.2, with the addition of a simulated foreground sample that matches with the flux-limited sample. We perform the cross-correlation for various redshift combinations of the κ map and the galaxy map, as well as the two shear catalogs. We find very good agreement between the two shear catalogs and between the simulation and data.

In Fig. 11, we show two examples of the measurements: cross-correlation of the METACALIBRATION κ maps at $0.63 < z < 0.9$ and $0.9 < z < 1.3$ with the flux-limited galaxy sample δ^g maps at $0.2 < z < 0.4$ and $0.4 < z < 0.6$, respectively. We show the data measurements together with the mean and standard deviation of the 12 measurements from the Buzzard simulations. Both the E-mode and the B-mode cross-correlation show excellent agreement between the data and the simulations. As the amplitude of the cross-correlation is sensitive to the cosmological model, galaxy bias, and the photo-z, the agreement between simulations and data suggests that there is no outstanding differences between the simulations and the data that could be potentially a sign of systematic effects.

Next, we measure the cross-correlation of the same κ maps with foreground REDMAGIC samples. We construct the samples so that the mean and spread of the $n(z)$ distribution is similar to that of the flux-limited sample. This corresponds to a redshift selection of $0.15 < z < 0.45$ ($0.25 < z < 0.6$) for the flux-limited sample at $0.2 < z < 0.4$ ($0.4 < z < 0.6$). By doing this, the ratio of the cross-correlation amplitude for the REDMAGIC sample and the flux-limited sample would scale directly as the ratio of the galaxy bias for the two samples. The cross-correlation between the κ maps and the REDMAGIC sample is also shown in Fig. 11. The error bars for the REDMAGIC sample are larger due to the lower number density, but overall the shape of the cross-correlation as a function of scale is very similar, with an overall multiplicative factor that is nearly constant over scales. The value of the multiplicative factor (within the 15–100 arcminute range) is ~ 1.38 for the lower redshift bin $0.2 < z < 0.4$ and ~ 1.27 for the higher redshift bin $0.4 < z < 0.6$. Crocce et al. (2016) measured the galaxy bias for a flux-limited galaxy sample in the DES SV data using an-
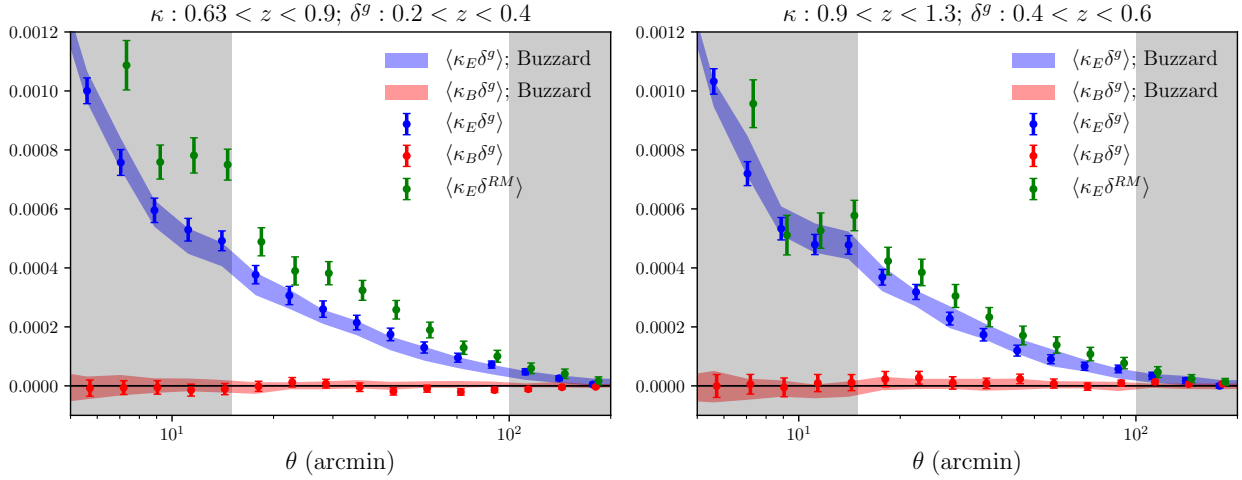
Figure 11. Cross-correlation of the κ maps with foreground galaxy samples. The blue (red) data points show the cross-correlation between the κ_E (κ_B) map with the foreground flux-limited sample for two redshift bins. The shaded band show the mean and standard deviation of the 12 Buzzard simulations, while the data points show the DES Y1 data. The green data points show $\langle\kappa_E\delta^{RM}\rangle$, the cross-correlation of the same κ_E maps with the foreground REDMAGIC sample which have similar redshift distributions as the two flux-limited samples but higher galaxy bias (therefore higher amplitudes). The grey shaded region is not used for the calculation of galaxy bias.
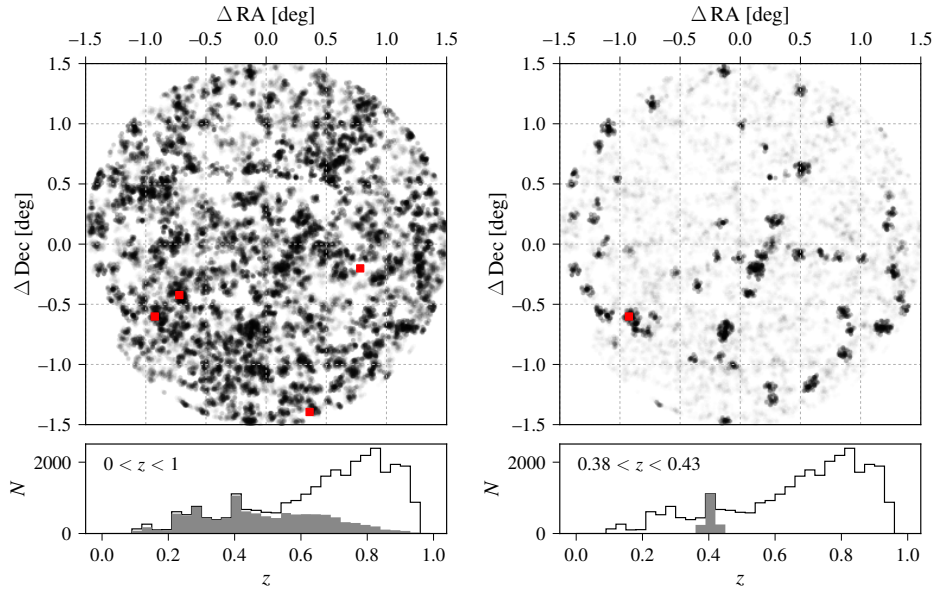
Figure 12. This figure shows the cluster galaxy distribution around the biggest overdensity in Fig. 8 at (RA, Dec) = (309°, −56°). We show in the left panels all members of REDMAPPER-detected galaxy clusters with $0 < z < 1$ and $\lambda > 5$. The top panel is the spatial distribution, projected onto the tangent plane, with shading of each circle indicating the lensing weights. The red dots indicate SPT-detected galaxy clusters from Bleem et al. (2015) in the same redshift range. The bottom panel is the redshift distribution of the cluster member galaxies, before (light) and after (dark) applying the lensing weights. The right panels show the same as the left panels, but for a narrower redshift range of $z = 0.405 \pm 0.025$, isolating the galaxies associated with a noticeable peak in the redshift distribution. The spatial distribution of the cluster members in this narrow redshift range exhibits some hint of a filamentary structure.

gular clustering measurements; their results give a bias of ~ 1.16 (~ 1.29) if we interpolate onto the redshift and magnitude range of our sample at $0.2 < z < 0.4$ ($0.4 < z < 0.6$). Kwan et al. (2017) measured the galaxy bias for the REDMAGIC sample to be ~ 1.6 using joint constraints from galaxy clustering and galaxy-galaxy lensing in approximately the redshift range of our data (the redshift evolution between the two lens bins considered is much less than the statistical uncertainties at ~ 0.3). The ratio of the galaxy bias

between the two samples is thus ~ 1.38 and 1.24 for the two redshift bins, which is broadly consistent with our measurements.

We defer a more quantitative analysis of galaxy bias to future work, but this initial test demonstrates one example of cross-correlation of the mass maps with other maps. The results also serve as a test for potential systematics in the mass maps – by comparing the measurements with simulations, we have shown that there is no outstanding systematic issues in using the maps for cross-correlation applications.

7.2   Peaks and voids

Another strength of map-level products is that one can visualise and detect pronounced local over- or underdense regions that would otherwise be averaged over in global summary statistics. The abundance of the massive peaks is a sensitive cosmological probe, as they occupy the highest end of the halo mass function (Bahcall & Fan 1998; Haiman et al. 2001; Holder et al. 2001). Some of the extreme structures can also help to constrain a certain class of modified gravity theories (Knox et al. 2006; Jain & Khoury 2010). On the other hand, the abundance of large voids has been used as a powerful test of ΛCDM cosmology (Plionis & Basilakos 2002; Higuchi & Inoue 2017). In this section we seek to briefly characterise the physical nature of peaks and voids that are associated with the largest over- or underdense regions in the convergence maps.

To construct a catalog of peaks and voids, we begin with the 4 tomographic S/N maps presented in Fig. 7, which are smoothed with a $\sigma_G = 30$ arcminutes Gaussian filter. We place a threshold on the pixels value at 2.5σ (S/N> 2.5 for peaks and $S/N < -2.5$ for voids), and for all pixels that survive the cut, we use a mean-shift clustering algorithm (Comaniciu & Meer 2002) to divide them into clusters of adjoining pixels. We inspect these clusters visually and place an additional cut requiring there to be more than 50 pixels (slightly larger than the smoothing we applied) in order to become a candidate for a peak or a void. In this approach, we find 9 (5), 9 (5), 18 (13) and 9 (7) peaks (voids) in the four tomographic maps, respectively.

To study the structures associated with peaks, we make use of the approach presented in Melchior et al. (2015). We select all cluster member galaxies of REDMAPPER clusters with richness $\lambda > 5$ within 1.5 degrees of the peak centre. We show their distribution around the largest peak in the map of Fig. 8 in the left panel of Fig. 12 at (RA, Dec)=(309°, -56°). While some correlated structure appears present in the 2D distribution, the redshift distributions of the cluster galaxies in this region appears to be very broad, even after taking the lensing kernel into account. This suggests that the large peak cannot be accounted for by one large structure localised in redshift space. In the right panel of Fig. 12 we isolate a particular peak at $z \approx 0.4$ in the redshift distribution and select only REDMAPPER clusters with $z = 0.4 \pm 0.025$, a range that corresponds to about two standard deviations of their typical redshift accuracy (Rykoff et al. 2016). A central, possibly filamentary structure becomes more pronounced, but there is no evidence of a particularly massive galaxy cluster or even a super-cluster in that region. In fact, of the four SPT-detected clusters from Bleem et al. (2015) within the search radius, only one, with $z \approx 0.4$, falls in this redshift range.

Performing an analogous analysis at different redshifts or on other peaks yields similar results, namely that overdensities smoothed on such a large scale generally do not correspond to massive structures in physical contact. Instead, the broad redshift kernel is prone to accumulating multiple layers of mildly overdense structures along the line of sight. This outcome demonstrates the difficulty of detecting clusters in weak-lensing mass maps or shear catalogs, especially when the number density of source galaxies is low and one cannot go to a smaller smoothing scale. This generally needs the construction of optimal matched filters in configuration and redshift space (Maturi et al. 2005; Simon et al. 2009; VanderPlas et al. 2011), which is outside of the scope of this work.

For voids the situation is more promising. We use REDMAGIC galaxies with relatively good photo-z's (same as that used in Sec. 7.1) as tracers of the foreground matter density and study
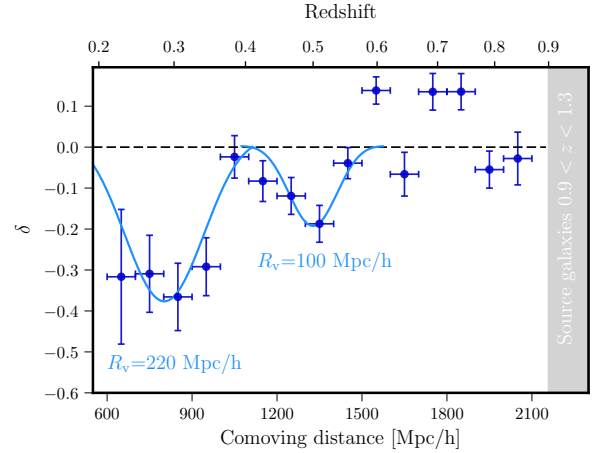
Figure 13. The data points show the REDMAGIC galaxy density contrast δ along the foreground line-of-sight of the largest void identified in the mass map in the highest redshift bin. The profile fits very well with a model consisting two supervoids with a size of 220 and 100 h^{-1}Mpc, as shown with the cyan line.

their radial distribution. We project the data into 2D slices of 50 h^{-1}Mpc along the line-of-sight. We then measure the density contrast of the REDMAGIC galaxies in these 2D slices where the large voids in the maps (significant negative convergence values) are measured, compared to the mean REDMAGIC density at that redshift. The density contrast measurements at different redshifts are then used to reconstruct the radial density profile of voids. As an example, we look at the largest void detected in the furthest $0.9 < z < 1.3$ bin at (RA, Dec)=(62°, -43°), and count galaxies within 2.0 degrees of the void centre, which approximately corresponds to the full angular size of the void in the map. We show the resulting line-of-sight density profile measurements of the REDMAGIC galaxies in Fig. 13. We find two extended underdensities that are consistent with supervoids of radii R_v=100 h^{-1}Mpc and R_v=220 h^{-1}Mpc assuming simple Gaussian void profiles (Finelli et al. 2016; Kovács & García-Bellido 2016; Sánchez et al. 2017). These supervoids are quite shallow even in their centres but their size is comparable to the largest known supervoids. Most probably, these supervoids have substructure at smaller scales but that information is not accessible even using high quality photo-z data like REDMAGIC.

We repeated the above analysis for less significant and less extended voids, finding that voids identified in the mass maps that extend beyond ∼0.64 deg² of size can typically be associated with at least one $R_v \gtrsim 100$ h^{-1}Mpc supervoid in the REDMAGIC catalogue. These are of greatest interest in cosmology and their integrated Sachs-Wolfe imprint was also studied using DES Y1 data (see e.g. Kovács et al. 2017).

8   CONCLUSION

Weak lensing allows us to probe the total mass distribution in the Universe. One of the most intuitive ways to visualise and comprehend this information is through weak lensing convergence maps, or mass maps. These maps contain the Gaussian and non-Gaussian information for the matter field, which could then either be extracted via various statistical tools, or analyzed locally for regions of special interest.

In this paper, we construct weak lensing mass maps for the first year of Dark Energy Survey data (DES Y1) using two independent shear catalogs, METACALIBRATION and IM3SHAPE, in the redshift range $0.2 < z < 1.3$ and in the region overlapping with the South Pole Telescope footprint. This yields maps covering $\sim 1,500$ deg^2, corresponding to a total volume of ≈ 10 Gpc^3. With the unprecedented large sky coverage, a spherical reconstruction approach was used based on decomposing the shear field into spin-2 spherical harmonics, followed by an E/B mode separation. The curl-free E-mode and the divergence-free B-mode form the E- and B-mode lensing convergence maps, κ_E and κ_B. The lensing potential ψ and deflection angles η can also be reconstructed using these decomposed spin harmonics.

We test the mass map reconstruction with simulations, starting with an idealised setup and gradually degrading the simulations to match the data. By doing so, we can isolate the effect of individual sources of systematics and noise. We use the F_1 and F_2 statistics (Eq. (17)) to quantify the performance of the reconstruction in terms of the amplitude and the phase information: for perfect reconstruction $F_1 = F_2 = 1$. Based on these statistics, we find that (1) we can reconstruct very well the convergence field in a fully-sampled, full-sky Gaussian simulation for scales larger than the pixel scale, as expected; (2) the DES Y1 mask biases the reconstructed maps at the few percent level, but the bias mainly comes from the pixels around the edges; (3) finite sampling from galaxies at the DES Y1 density does not degrade the reconstruction significantly for our maps at a resolution of 3.44 arcminutes; (4) adding shape noise increases the variance of the map and perturbs the phase information, but at the DES Y1 noise level, the signal-to-noise is still significant and the resulting F_1 and F_2 are consistent with 1; (5) we can reconstruct within measurement uncertainty the second moment of the maps on all scales and third moment of the maps for scales > 5 arcminutes, where shape noise is subdominant.

One new application that comes with the large sky coverage is the reconstruction of other lensing maps such as the lensing potential ψ and deflection angles η maps. We explore briefly in Appendix B this application, finding a $\sim 70\%$ ($\sim 50\%$) lower amplitude in the reconstruction for ψ (η). The reconstruction of ψ and η is relatively poor compared to that of the κ maps because information in η is dominated by scales larger than κ, and the information in ψ is dominated by even larger scales. This suggests that from κ to η to ψ, the importance of the mask increases while the importance of shot noise and shape noise decreases.

After rigorous testing with simulations, we generate weak lensing mass maps from the DES Y1 data with a spatial resolution of ~ 3.44 arcminutes. We construct one map that covers the entire redshift range of $0.2 < z < 1.3$, which carries the highest S/N, and also four tomographic bins at the redshift intervals $0.2 < z < 0.43$, $0.43 < z < 0.63$, $0.63 < z < 0.9$, and $0.9 < z < 1.3$. The tomographic maps are relatively noisy, but allow us to explore the redshift-dependencies of the maps and can be used for tomographic cross-correlation with other tracers of mass. In the highest signal-to-noise map (METACALIBRATION, $0.2 < z < 1.3$), the ratio between the mean S/N in the E-mode and the B-mode map is ~ 1.5 (~ 2) when smoothed with a Gaussian filter of $\sigma_G = 30$ (80) arcminutes. We examine the PDF of the maps, together with the second and third moments of the PDF as a function of smoothing scale and find them to be consistent with realistic simulations that incorporate similar noise and mask properties as the data. We further test for systematic effects by cross-correlating the maps with various environment and PSF quantities at the one-point and two-

point level. We find no significant systematic contamination of the maps beyond what is expected from statistical fluctuations.

Finally, we demonstrate two applications of these mass maps. First, we cross-correlate the mass maps with two sets of foreground mass tracers constructed to have similar redshift distributions: a flux-limited galaxy sample and an LRG sample. The cross-correlation is done in two redshift bins and shows very good agreement with simulations. The ratio of the amplitudes of the cross-correlation, which reflects the ratio of the galaxy bias for the two samples, are consistent with previous measurements of similar samples in earlier DES data. Second, we examine the extreme peaks and voids identified in the maps. We find that most high S/N peaks in the maps correspond to an accumulated mass distribution along the line of sight, even though rare filamentary structures could be found occasionally. For the high-S/N voids, however, most of them correspond to real void structures with $R_v \gtrsim 100 \ h^{-1}$Mpc in the foreground.

The DES Y1 mass maps are the largest weak lensing mass maps to date constructed from galaxy surveys, about ten times larger than the previous maps from CFHTLenS (Van Waerbeke et al. 2013) and DES SV (Vikram et al. 2015; Chang et al. 2015). Even though the Y1 depth is shallower (and therefore noisier) than the previous maps, these very large maps provide a new perspective on weak lensing map making and the various topics one can explore with them. Moving onto the larger dataset from DES and other surveys, we expect many of the explorations in this paper to be carried out and advanced to serve as complementary probes of cosmology alongside more traditional two-point statistics.

REFERENCES

Abbott T., et al., 2016, Phys.Rev.D, 94, 022001
Aihara H., et al., 2017, preprint, (arXiv:1702.08449)
Bahcall N. A., Fan X., 1998, ApJ, 504, 1
Bartelmann M., 2010, Classical and Quantum Gravity, 27, 233001
Bartelmann M., Schneider P., 2001, Physics Reports, 340, 291
Becker M. R., 2013, MNRAS, 435, 115
Benítez N., 2000, ApJ, 536, 571
Bernardeau F., van Waerbeke L., Mellier Y., 1997, A&A, 322, 1
Blazek J., Vlah Z., Seljak U., 2015, JCAP, 8, 015
Bleem L. E., et al., 2015, ApJS, 216, 27
Bonnett C., et al., 2016, Phys.Rev.D, 94, 042005
Bruderer C., Chang C., Refregier A., Amara A., Bergé J., Gamper L., 2016, ApJ, 817, 25
Bruzual G., Charlot S., 2003, MNRAS, 344, 1000
Carlstrom J. E., et al., 2011, PASP, 123, 568

Castro P. G., Heavens A. F., Kitching T. D., 2005, Phys.Rev.D, 72, 023516
Cawthon R., et al., 2017, in prep.
Chang C., Jain B., 2014, MNRAS, 443, 102
Chang C., et al., 2015, Physical Review Letters, 115, 051301
Chang C., et al., 2016, MNRAS, 459, 3203
Clerkin L., Kirk D., Lahav O., Abdalla F. B., Gaztañaga E., 2015, MNRAS, 448, 1389
Clowe D., Bradač M., Gonzalez A. H., Markevitch M., Randall S. W., Jones C., Zaritsky D., 2006, ApJ, 648, L109
Coe D., Benítez N., Sánchez S. F., Jee M., Bouwens R., Ford H., 2006, AJ, 132, 926
Coleman G. D., Wu C.-C., Weedman D. W., 1980, ApJS, 43, 393
Comaniciu D., Meer P., 2002, IEEE Transactions on Pattern Analysis and Machine Intelligence, 24, 603
Conroy C., Wechsler R. H., Kravtsov A. V., 2006, ApJ, 647, 201
Cooper M. C., 2006, in American Astronomical Society Meeting Abstracts. p. 1159
Cooray A., Hu W., 2001, ApJ, 548, 7
Crocce M., Pueblas S., Scoccimarro R., 2006, MNRAS, 373, 369
Crocce M., Castander F. J., Gaztañaga E., Fosalba P., Carretero J., 2015, MNRAS, 453, 1513
Crocce M., et al., 2016, MNRAS, 455, 4301
DES Collaboration et al., 2017, to be submitted to Phys. Rev. D
Dark Energy Survey Collaboration et al., 2016, MNRAS, 460, 1270
Davis C., et al., 2017, in prep.
Dietrich J. P., Hartlap J., 2010, MNRAS, 402, 1049
Dodelson S., Zhang P., 2005, Phys.Rev.D, 72, 083001
Dodelson S., Schmidt F., Vallinotto A., 2008, Phys.Rev.D, 78, 043508
Drlica-Wagner A., et al., 2017, submitted to Astrophys. J. Suppl. Ser.
Elvin-Poole J., et al., 2017, to be submitted to Phys. Rev. D
Erben T., et al., 2013, MNRAS, 433, 2545
Fenech Conti I., Herbonnet R., Hoekstra H., Merten J., Miller L., Viola M., 2016, preprint, (arXiv:1606.05337)
Finelli F., García-Bellido J., Kovács A., Paci F., Szapudi I., 2016, MNRAS, 455, 1246
Flaugher B., 2005, International Journal of Modern Physics A, 20, 3121
Flaugher B., et al., 2015, AJ, 150, 150
Fosalba P., Gaztañaga E., Castander F. J., Manera M., 2008, MNRAS, 391, 435
Fosalba P., Gaztañaga E., Castander F. J., Crocce M., 2015a, MNRAS, 447, 1319
Fosalba P., Crocce M., Gaztañaga E., Castander F. J., 2015b, MNRAS, 448, 2987
Gatti M., et al., 2017, in prep.
Gaztanaga E., Bernardeau F., 1998, A&A, 331, 829
Górski K. M., Hivon E., Banday A. J., Wandelt B. D., Hansen F. K., Reinecke M., Bartelmann M., 2005, ApJ, 622, 759
Haiman Z., Mohr J. J., Holder G. P., 2001, ApJ, 553, 545
Hand N., et al., 2015, Phys.Rev.D, 91, 062001
Heavens A., 2003, MNRAS, 343, 1327
Heavens A. F., Kitching T. D., Taylor A. N., 2006, MNRAS, 373, 105
Higuchi Y., Inoue K. T., 2017, preprint, (arXiv:1707.07535)
Hildebrandt H., et al., 2017, MNRAS, 465, 1454
Holder G., Haiman Z., Mohr J. J., 2001, ApJ, 560, L111
Hoyle B., et al., 2017, to be submitted to Mon. Not. R. Astron. Soc.
Huff E., Mandelbaum R., 2017, preprint, (arXiv:1702.02600)
Jain B., Khoury J., 2010, Annals of Physics, 325, 1479
Jain B., Seljak U., 1997, ApJ, 484, 560
Jain B., Van Waerbeke L., 2000, ApJ, 530, L1
Jarvis M., et al., 2015, preprint, (arXiv:1507.05603)
Kacprzak T., Zuntz J., Rowe B., Bridle S., Refregier A., Amara A., Voigt L., Hirsch M., 2012, MNRAS, 427, 2711
Kacprzak T., et al., 2016, MNRAS, 463, 3653
Kaiser N., Squires G., 1993, ApJ, 404, 441
Kinney A. L., Calzetti D., Bohlin R. C., McQuade K., Storchi-Bergmann T., Schmitt H. R., 1996, ApJ, 467, 38
Kirk D., Abdalla F. B., Benoit-Lévy A., Bull P., Joachimi B., 2015, Ad-

vancing Astrophysics with the Square Kilometre Array (AASKA14), p. 20

Kirk D., et al., 2016, MNRAS, 459, 21

Kitching T. D., et al., 2014, MNRAS, 442, 1326

Knox L., Song Y.-S., Tyson J. A., 2006, Phys.Rev.D, 74, 023512

Kovács A., García-Bellido J., 2016, MNRAS, 462, 1882

Kovács A., et al., 2017, MNRAS, 465, 4166

Kratochvil J. M., Haiman Z., May M., 2010, Phys.Rev.D, 81, 043519

Kwan J., et al., 2017, MNRAS, 464, 4045

Leistedt B., McEwen J. D., Büttner M., Peiris H. V., 2017, MNRAS, 466, 3728

Leonard A., Lanusse F., Starck J.-L., 2014, MNRAS, 440, 1281

Lewis A., Bridle S., 2002, Phys.Rev.D, 66, 103511

Liu J., Hill J. C., 2015, Phys.Rev.D, 92, 063517

MacCrann N., et al., 2017, in prep.

Mandelbaum R., et al., 2017, preprint, (arXiv:1705.06745)

Manzotti A., et al., 2017, preprint, (arXiv:1701.04396)

Marian L., Bernstein G. M., 2007, Phys.Rev.D, 76, 123009

Marshall P. J., Hobson M. P., Gull S. F., Bridle S. L., 2002, MNRAS, 335, 1037

Massey R., et al., 2007, ApJS, 172, 239

Maturi M., Meneghetti M., Bartelmann M., Dolag K., Moscardini L., 2005, A&A, 442, 851

Melchior P., et al., 2015, MNRAS, 449, 2219

Melchior P., et al., 2017, MNRAS, 469, 4899

Oguri M., et al., 2017, preprint, (arXiv:1705.06792)

Patton K., Blazek J., Honscheid K., Huff E., Melchior P., Ross A. J., Suchyta E., 2016, preprint, (arXiv:1611.01486)

Pires S., Starck J.-L., Amara A., Teyssier R., Réfrégier A., Fadili J., 2009, MNRAS, 395, 1265

Planck Collaboration et al., 2016, A&A, 594, A13

Plionis M., Basilakos S., 2002, MNRAS, 330, 399

Prat J., et al., 2017, to be submitted to Phys. Rev. D

Pujol A., et al., 2016, MNRAS, 462, 35

Reddick R. M., Wechsler R. H., Tinker J. L., Behroozi P. S., 2013, ApJ, 771, 30

Refregier A., Kacprzak T., Amara A., Bridle S., Rowe B., 2012, MNRAS, 425, 1951

Rykoff E. S., et al., 2016, ApJS, 224, 1

Sánchez C., et al., 2017, MNRAS, 465, 746

Schneider P., 1996, MNRAS, 283, 837

Seitz S., Schneider P., Bartelmann M., 1998, A&A, 337, 325

Sheldon E. S., 2014, MNRAS, 444, L25

Sheldon E. S., Huff E. M., 2017, preprint, (arXiv:1702.02601)

Shirasaki M., Horiuchi S., Yoshida N., 2014, Phys.Rev.D, 90, 063502

Simon P., Taylor A. N., Hartlap J., 2009, MNRAS, 399, 48

Springel V., 2005, MNRAS, 364, 1105

Troxel M. A., Ishak M., 2015, Physics Reports, 558, 1

Troxel M. A., et al., 2017, to be submitted to Phys. Rev. D

Vallinotto A., Dodelson S., Schimd C., Uzan J.-P., 2007, Phys.Rev.D, 75, 103509

Van Waerbeke L., et al., 2013, MNRAS, 433, 3373

VanderPlas J. T., Connolly A. J., Jain B., Jarvis M., 2011, ApJ, 727, 118

Vikram V., et al., 2015, Phys.Rev.D, 92, 022006

Wallis C. G. R., McEwen J. D., Kitching T. D., Leistedt B., Plouviez A., 2017, preprint, (arXiv:1703.09233)

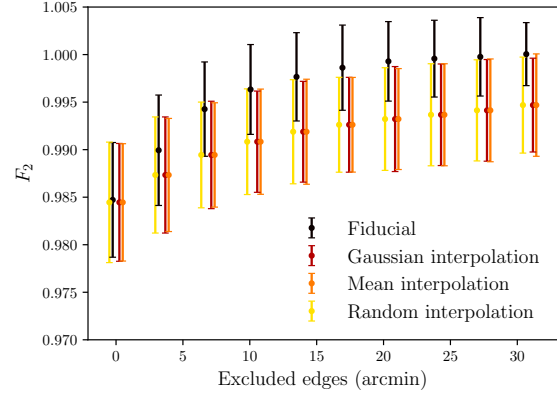Yu B., Hill J. C., Sherwin B. D., 2017, preprint, (arXiv:1705.02332)

Zuntz J., Kacprzak T., Voigt L., Hirsch M., Rowe B., Bridle S., 2013, MNRAS, 434, 1604

Zuntz J., et al., 2015, Astronomy and Computing, 12, 45

Zuntz J., et al., 2017, submitted to Mon. Not. R. Astron. Soc.

de Jong J. T. A., et al., 2015, A&A, 582, A62

von der Linden A., et al., 2014, MNRAS, 439, 2

Figure A1. $F_2 = \langle \kappa_E \kappa_{\mathrm{sm}} \rangle / \langle \kappa_{\mathrm{sm}}^2 \rangle$ for different interpolation schemes for empty pixels inside the footprint.

APPENDIX A: INTERPOLATING EMPTY PIXELS

In this appendix we test the impact of the empty pixels inside the contiguous footprint and different approaches to interpolate over them. We use the same noiseless Buzzard simulations used in Sec. 5.2 and test with the redshift bin of $0.2 < z < 1.3$. In this map, the fraction of empty pixels inside the footprint occupies $\sim 1.67\%$ of the total pixels.

We test the following 4 approaches of assigning values to these empty pixels and calculate the F_1 and F_2 statistics defined in Sec. 5:

- Fiducial: set the empty pixels to 0.
- Gaussian interpolation: interpolate the values of these empty pixels from a Gaussian kernel with a σ corresponding to 3 times the pixel size.
- Mean interpolation: we assign the empty pixels the mean value of their neighbour pixels.
- Random interpolation: we assign the empty pixels the value of a random neighbour pixel.

In Fig. A1 we show the F_2 statistics as a function of the scale excluded from the edges for all this cases, similar to Fig. 2. The F_1 statistics looks qualitatively similar to F_2. We see that at our resolution, the different approaches all give very similar results. We therefore adopt the fiducial approach for simplicity in our main analysis.

## APPENDIX B: RECONSTRUCTING THE LENSING POTENTIAL AND DEFLECTION MAP

As discussed in Sec. 2, in addition to the convergence maps κ, we can also construct the lensing potential ψ and deflection η maps with similar formalism. In this appendix we show the implementation of the reconstruction for ψ and η. We perform in Appendix B1 similar tests on the reconstruction with simulations as in Sec. 5.1. Then we apply the method to DES Y1 data in Appendix B2. Although the quality of the reconstruction for ψ and η is not comparable to that of the κ maps, they point to an area that we can start to explore as the sky coverage of future weak lensing data sets becomes increasingly large.
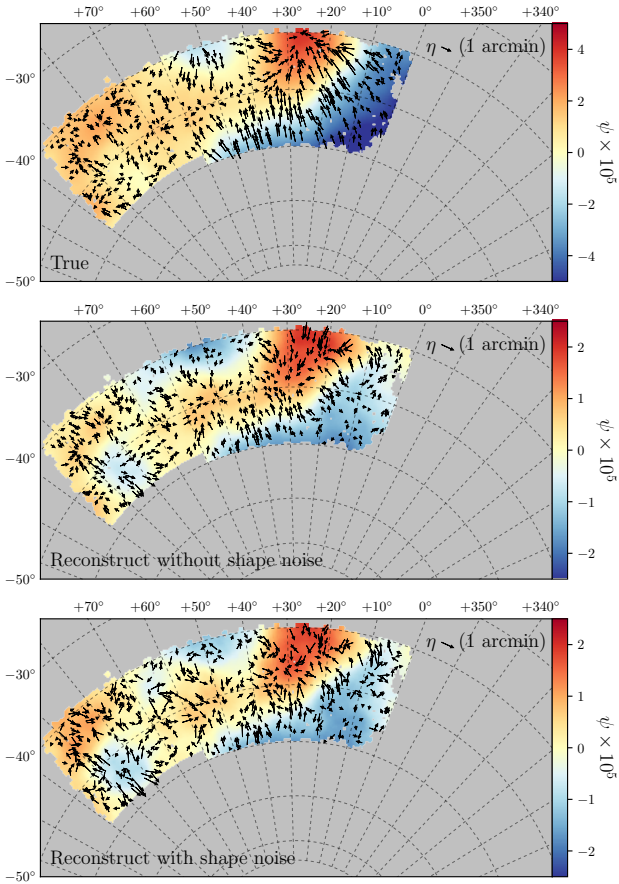
Figure B1. The truth (top), noiseless reconstruction (middle) and noisy reconstruction (bottom) of ψ and η field using the Gaussian simulations and a Y1-like mask. The colours indicate the value of the ψ fields while the arrows indicate the observed deflection angle caused by lensing. The arrows are not to-scale — they are enlarged for visualisation purpose. The amplitude of the reconstructed field is lower than the true field, therefore the colour bars in the bottom panel span over a range 4 times smaller than the top panel; while the arrows in the bottom panel are enlarged 2 times more than the top panel, as indicated by the one-arcminute bar on the upper right.

B1   Simulation tests

Similar to our test in reconstructing the convergence maps in Sec. 5, we investigate the performance of reconstructing the lensing potential field ψ and the deflection field η. The techniques used for mapping these quantities are similar to those used for κ and utilise the HEALPIX routines. The definition of η has been introduced in Eq. (10) and related to ψ in Eq. (11), but as η is a spin-1 field it requires use of the HEALPIX routine `alm2map_spin` function to produce the final maps. In Fig. B1 we show an example of a ψ and η map generated via `synfast`. The top panel displays the true fields; the middle panel shows a reconstructed field with the Y1 mask imposed and $RA > 100°$ region excluded; the bottom panel shows the reconstruction with the mask and realistic Y1 shape noise. We find that both the ψ and η fields exhibit significant degradation due to the mask, as shown in the difference between the upper two panels, even though some level of resemblance remains. The addition of shape noise has a much less significant effect, as can be seen from the bottom panel, which is very similar to the middle panel; this is
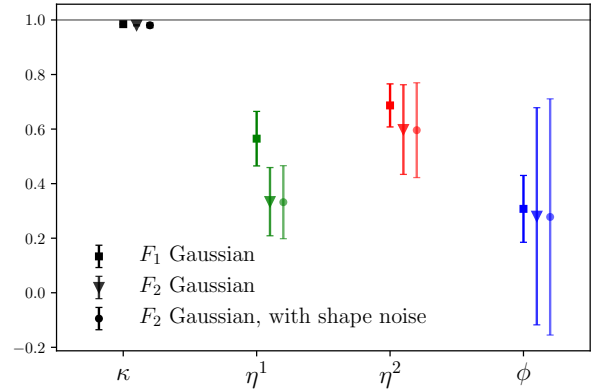
Figure B2. F_1 (square markers) and F_2 (triangle markers) statistics for the reconstruction of the κ (black), $\eta = (\eta^1, \eta^2)$ (green and red) and ψ (blue) fields measured excluding pixels within ~ 10 arcminutes from the edge of the mask. All measurements are done with the Gaussian simulations and the Y1-like mask described in Sec. 5.1. The round markers are the same as the triangle markers except for the addition of shape noise.

expected as shape noise mainly degrades small-scale information, and is less important for the reconstruction of the ψ and η maps.

To quantify the degradation caused by the mask, we calculate the F_1 and F_2 (replacing κ by ψ and η in Eq. (17)) when excluding 10 arcminutes from the edges as shown in Fig. B2. We generate 500 Gaussian realisations of the sky with the same underlying power spectrum to account for the effect of cosmic variance, which is an important factor in the reconstruction of ψ and η since the information is dominated by large scales. We show the mean and standard deviation from these 500 simulations in Fig. B2. As expected, we find that the mask has a stronger effect upon these two maps than for κ, as they use a higher proportion of information from the lower ℓ modes, which are more poorly constrained. This can be seen as a progressive degradation, from κ to η, to the most adversely affected ψ, but significant information is still reconstructed from the maps. The main effect of the mask on ψ can be seen from the low value of F_1, due to the large unobserved sky regions suppressing the power inside the masked region by $\sim 70\%$. Similarly, η also suffers from this but to a lesser extent; η^1 is suppressed by $\sim 60\%$ and η^2 by $\sim 40\%$. The difference in this amplitude suppression comes from the fact that η^1 and η^2 are reconstructing the deflection angle in different directions on the sky — the mask is a non-isotropic and there is more information in the RA direction, which contributes mainly to η^2.

To measure the reliability of the reconstruction of the phase information we use F_2. Comparing F_2 to F_1 gives a measurement of the phase reconstruction. These results are also shown in Fig. B2. We find that for both ψ and η, the mean F_2 is at a similar level as F_1, but the standard deviation of F_2 is much larger than that of F_1, which suggests that the quality of the phase reconstruction varies dramatically depending on the specific realisation of the sky. Furthermore, we find that the influence of shape noise on F_2 is much less compared to the influence from the mask, as also suggested by Fig. B1.

Taken in combination, F_1 and F_2 suggest that considerable information can be inferred about η and ψ, although with much larger uncertainties than for κ. We do not perform further quantitative analyses on these maps, but note that for data sets on areas larger than DES Y1, the reconstruction of these other lensing fields becomes interesting. In these scenarios, algorithms that

specifically deal with the mask will be particularly useful. For example, instead of converting the γ field to ψ and η directly, one can imagine forward-modelling the observed γ field from some underlying ψ field. We defer the study of a forward-fitting mass mapping method to future work.

B2 Deflection and potential maps for DES Y1

We now apply the reconstruction method above to DES Y1 data. In Fig. B3 we show these maps constructed using METACALIBRA-TION shear measurements with the full redshift range $0.2 < z < 1.3$. As can be seen from the simulation tests in the previous section, the amplitude of these maps are expected to be much lower than the true fields due to the effect of masking. However, we can see reasonable correspondence between all the three maps: κ, η and ψ. On large scales, we find the low convergence (underdensed) regions are mostly located on the upper half of the footprint in Fig. 6: those correspond to a high potential value in Fig. B3, and the deflection angle points from low to high potential. The characteristic scale of ψ is larger than η, which is larger than κ. The amplitude of the ψ and η map also agrees well with that expected from the simulation tests in the previous section — the potential field is $\sim 10^{-4}$ and the deflection angle has a value on the order slightly below an arcminute. This map has implications for the mass distribution beyond the footprint. For example, the fact that the deflection angle points away from the boundary at the lower boundary of the map at RA$\sim 30°$ could indicate a large-scale overdensity just outside the footprint, which will be tested when more data is available.

APPENDIX C: CATALOG CONSISTENCY

In this appendix we compare maps from IM3SHAPE catalog with the results presented in the main text from METACALIBRATION. We also compare with the map from DES Science Verification data (SV, Vikram et al. 2015; Chang et al. 2015) which partly overlaps with the Y1 footprint.

In Fig. C1 and Fig. C2 we show the convergence maps generated using the IM3SHAPE shear catalogs. Comparing to Fig. 6 and Fig. 7 ,we can see that the broad structures in the κ_E maps are similar, especially for the high S/N maps. The contrast between the E- and B-mode is less strong compared to METACALIBRATION due to the overall lower S/N in the IM3SHAPE catalog. Nevertheless, the agreement between the two independent catalogs provides a check of the shear measurement pipeline.

In Fig. C3 we show the Y1 map and the SV map in the SV footprint; both maps use galaxies with a mean redshift $0.2 < z < 1.3$, and smoothed with $\sigma_G = 20$ arcminutes. The SV map was constructed using another independent catalog ngmix and a different photo-z code, SKYNET. The SV map is also half a magnitude deeper than the Y1 map. The visual correspondence between the structures in the two maps is very good given the differences in the input data. This again serves as a consistency check between the different catalogs.

APPENDIX D: AUTHOR AFFILIATIONS

[1]Kavli Institute for Cosmological Physics, University of Chicago, Chicago, IL 60637, USA

[2]DEDIP/DAP, IRFU, CEA, Université Paris-Saclay, F-91191 Gif-sur-Yvette, France

[3]Université Paris Diderot, AIM, Sorbonne Paris Cité, CEA, CNRS, F-91191 Gif-sur-Yvette, France

[4]Institut de Ciències de l'Espai, IEEC-CSIC, Campus UAB, Facultat de Ciències, Torre C5 par-2, 08193 Bellaterra, Barcelona, Spain

[5]Institute of Cosmology & Gravitation, University of Portsmouth, Portsmouth, PO1 3FX, UK

[6]Jodrell Bank Center for Astrophysics, School of Physics and Astronomy, University of Manchester, Oxford Road, Manchester, M13 9PL, UK

[7]Department of Astrophysical Sciences, Princeton University, Peyton Hall, Princeton, NJ 08544, USA

[8]Institut de Física d'Altes Energies (IFAE), The Barcelona Institute of Science and Technology, Campus UAB, 08193 Bellaterra (Barcelona) Spain

[9]Department of Physics and Astronomy, University of Pennsylvania, Philadelphia, PA 19104, USA

[10]New York University, CCPP, New York, NY 10003, USA

[11]Einstein Fellow

[12]Kavli Institute for Cosmology, University of Cambridge, Madingley Road, Cambridge CB3 0HA, UK

[13]Institute of Astronomy, University of Cambridge, Madingley Road, Cambridge CB3 0HA, UK

[14]Faculty of Physics, Ludwig-Maximilians-Universität, Scheinerstr. 1, 81679 Munich, Germany

[15]LSST, 933 North Cherry Avenue, Tucson, AZ 85721, USA

[16]Department of Physics, Stanford University, 382 Via Pueblo Mall, Stanford, CA 94305, USA

[17]Kavli Institute for Particle Astrophysics & Cosmology, P. O. Box 2450, Stanford University, Stanford, CA 94305, USA

[18]CNRS, UMR 7095, Institut d'Astrophysique de Paris, F-75014, Paris, France

[19]Department of Physics & Astronomy, University College London, Gower Street, London, WC1E 6BT, UK

[20]Sorbonne Universités, UPMC Univ Paris 06, UMR 7095, Institut d'Astrophysique de Paris, F-75014, Paris, France

[21]Laboratório Interinstitucional de e-Astronomia - LIneA, Rua Gal. José Cristino 77, Rio de Janeiro, RJ - 20921-400, Brazil

[22]Observatório Nacional, Rua Gal. José Cristino 77, Rio de Janeiro, RJ - 20921-400, Brazil

[23]Centro de Investigaciones Energéticas, Medioambientales y Tecnológicas (CIEMAT), Madrid, Spain

[24]Fermi National Accelerator Laboratory, P. O. Box 500, Batavia, IL 60510, USA

[25]SLAC National Accelerator Laboratory, Menlo Park, CA 94025, USA

[26]Department of Physics, ETH Zurich, Wolfgang-Pauli-Strasse 16, CH-8093 Zurich, Switzerland

[27]Jet Propulsion Laboratory, California Institute of Technology, 4800 Oak Grove Dr., Pasadena, CA 91109, USA

[28]Department of Physics, The Ohio State University, Columbus, OH 43210, USA

[29]Center for Cosmology and Astro-Particle Physics, The Ohio State University, Columbus, OH 43210, USA

[30]University of Arizona, Department of Physics, 1118 E. Fourth St., Tucson, AZ 85721, USA

[31]Brookhaven National Laboratory, Bldg 510, Upton, NY 11973, USA

[32]Max Planck Institute for Extraterrestrial Physics, Giessenbachstrasse, 85748 Garching, Germany

[33]Argonne National Laboratory, 9700 South Cass Avenue, Lemont, IL 60439, USA

[34]Institute for Astronomy, University of Edinburgh, Edinburgh EH9 3HJ, UK

[35]Cerro Tololo Inter-American Observatory, National Optical Astronomy
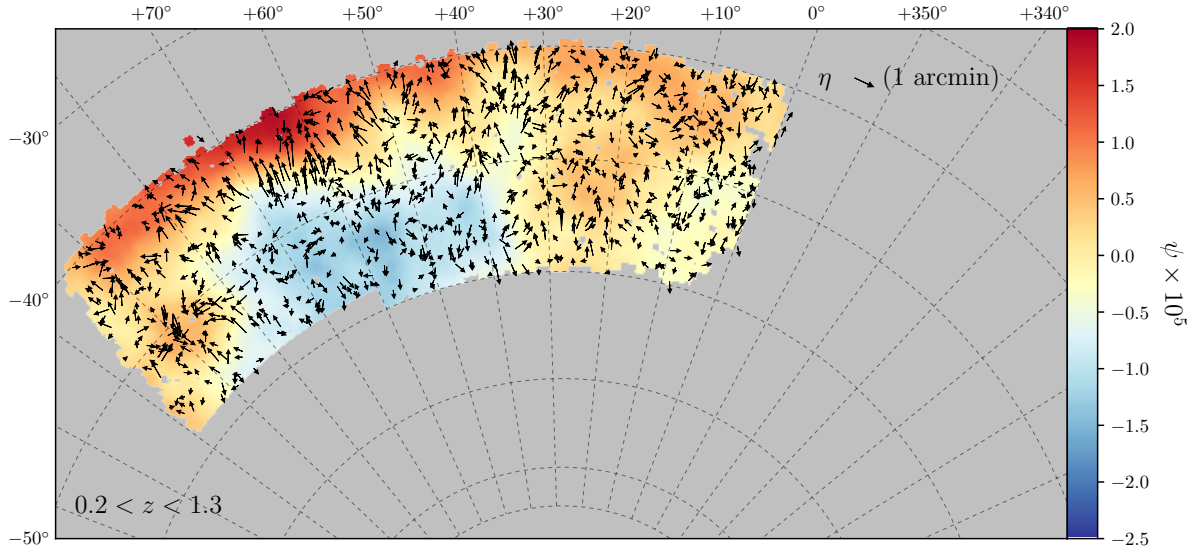
Figure B3. The lensing potential (colour map) and deflection field (arrows) reconstructed for the DES Y1 METACALIBRATION data in the redshift range $0.2 < z < 1.3$. The arrows are not to-scale, but can be compared to the one-arcminute arrow in the upper right corner.

Observatory, Casilla 603, La Serena, Chile

[36] Department of Physics and Electronics, Rhodes University, PO Box 94, Grahamstown, 6140, South Africa

[37] Department of Astronomy, University of Illinois, 1002 W. Green Street, Urbana, IL 61801, USA

[38] National Center for Supercomputing Applications, 1205 West Clark St., Urbana, IL 61801, USA

[39] Department of Physics, IIT Hyderabad, Kandi, Telangana 502285, India

[40] Excellence Cluster Universe, Boltzmannstr. 2, 85748 Garching, Germany

[41] Instituto de Fisica Teorica UAM/CSIC, Universidad Autonoma de Madrid, 28049 Madrid, Spain

[42] Astronomy Department, University of Washington, Box 351580, Seattle, WA 98195, USA

[43] Santa Cruz Institute for Particle Physics, Santa Cruz, CA 95064, USA

[44] Australian Astronomical Observatory, North Ryde, NSW 2113, Australia

[45] Departamento de Física Matemática, Instituto de Física, Universidade de São Paulo, CP 66318, São Paulo, SP, 05314-970, Brazil

[46] Institució Catalana de Recerca i Estudis Avançats, E-08010 Barcelona, Spain

[47] Department of Physics and Astronomy, Pevensey Building, University of Sussex, Brighton, BN1 9QH, UK
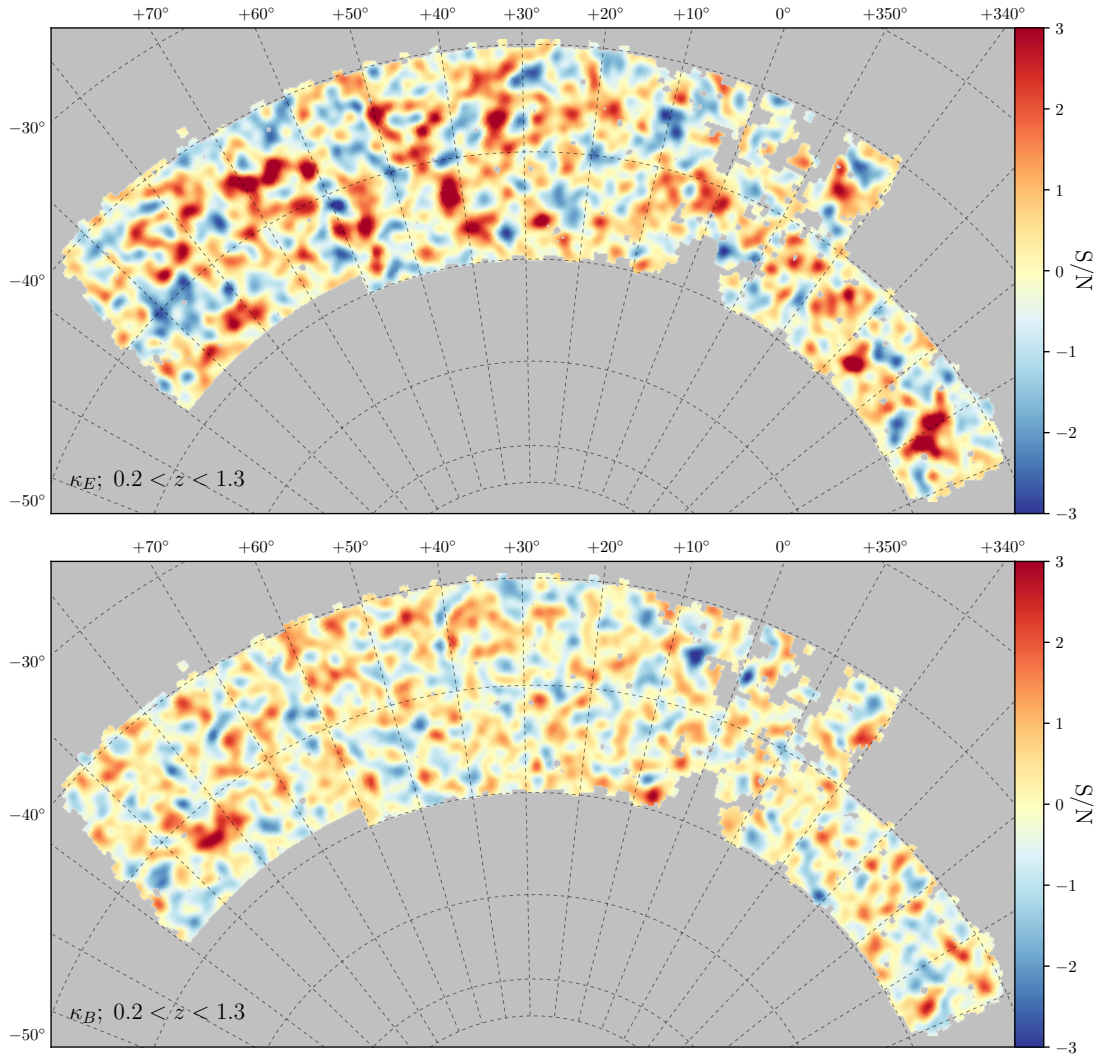
[48] Department of Physics, University of Michigan, Ann Arbor, MI 48109, USA

[49] School of Physics and Astronomy, University of Southampton, Southampton, SO17 1BJ, UK
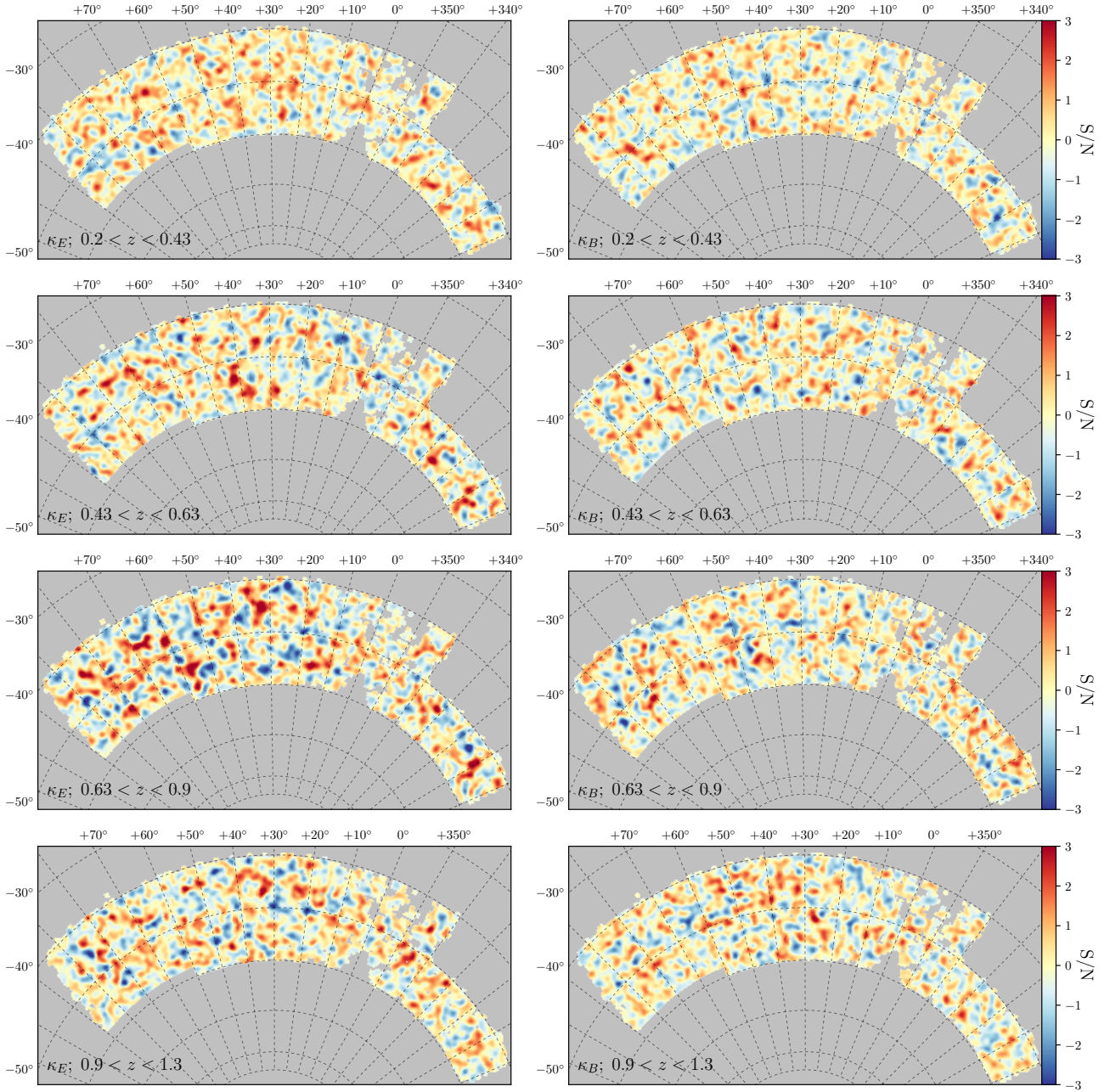
[50] Instituto de Física Gleb Wataghin, Universidade Estadual de Campinas, 13083-859, Campinas, SP, Brazil

[51] Computer Science and Mathematics Division, Oak Ridge National Laboratory, Oak Ridge, TN 37831
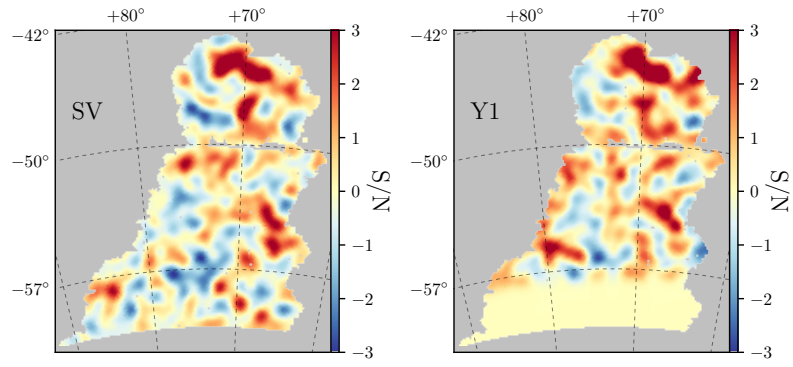
Figure C1. Same as Fig. 6, but constructed using the IM3SHAPE shear catalog.

Figure C2. Same as Fig. 7, but constructed using the IM3SHAPE shear catalog.

Figure C3. Convergence map constructed using the SV NGMIX catalog (left) and the Y1 METACALIBRATION catalog (right).